

## On the Relationship between Decadal Buoyancy Anomalies and Variability of the Atlantic Meridional Overturning Circulation

MARTHA W. BUCKLEY,\* DAVID FERREIRA, JEAN-MICHEL CAMPIN, JOHN MARSHALL,  
AND ROSS TULLOCH

*Massachusetts Institute of Technology, Cambridge, Massachusetts*

(Manuscript received 8 September 2011, in final form 29 February 2012)

### ABSTRACT

Owing to the role of the Atlantic meridional overturning circulation (AMOC) in ocean heat transport, AMOC variability is thought to play a role in climate variability on a wide range of time scales. This paper focuses on the potential role of the AMOC in climate variability on decadal time scales. Coupled and ocean-only general circulation models run in idealized geometries are utilized to study the relationships between decadal AMOC and buoyancy variability and determine whether the AMOC plays an active role in setting sea surface temperature on decadal time scales. Decadal AMOC variability is related to changes in the buoyancy field along the western boundary according to the thermal wind relation. Buoyancy anomalies originate in the upper ocean of the subpolar gyre and travel westward as baroclinic Rossby waves. When the buoyancy anomalies strike the western boundary, they are advected southward by the deep western boundary current, leading to latitudinally coherent AMOC variability. The AMOC is observed to respond passively to decadal buoyancy anomalies: although variability of the AMOC leads to meridional ocean heat transport anomalies, these transports are not responsible for creating the buoyancy anomalies in the subpolar gyre that drive AMOC variability.

### 1. Introduction

In a recent review paper, Lozier (2010) concluded that the most significant question concerning variability of the Atlantic meridional overturning circulation (AMOC) is the role of the AMOC in creating decadal SST anomalies. Furthermore, she noted that no observational study to date has successfully linked SST changes to AMOC variability.

The hypothesis that the AMOC plays an active role in decadal climate variability is rooted in the role of the AMOC in the mean meridional ocean heat transport (OHT). Due to the deep, interhemispheric overturning circulation in the Atlantic, commonly referred to as the AMOC, the Atlantic Ocean transports heat northward in both hemispheres. The Atlantic OHT peaks at a value of about 1 PW at 20°N (Trenberth and Caron 2001; Ganachaud and Wunsch 2003), and observational (Talley 2003) and modeling (Boccaletti et al. 2005; Ferrari and

Ferreira 2011) studies suggest about 60% of the peak OHT can be attributed to the AMOC. Thus, the AMOC plays a role in maintaining the current mean climate, and it has been suggested that its variability may play a role in climate variability on a wide range of time scales.

Observations of decadal SST variability from the instrumental record (Bjerknes 1964; Kushnir 1994; Knight et al. 2005; Ting et al. 2009) and climate proxy data (Mann et al. 1995, 1998) are a second piece of evidence that the ocean may play an active role in decadal climate variability. The basin-scale nature of observed decadal SST anomalies led Bjerknes (1964) and Kushnir (1994) to hypothesize that these anomalies are due to changes in meridional OHT. A number of studies have attempted to test this hypothesis by analyzing the relationships between decadal SST anomalies and the state of the overlying atmosphere. While it is well established that on interannual time scales SST variability is primarily forced by local atmospheric variability (Hasselmann 1976; Cayan 1992a,b), the relative roles of atmospheric forcing and ocean dynamics in setting SST on decadal time scales are not known. Deser and Blackmon (1993) and Seager et al. (2000) argue that the majority of wintertime SST variability observed during the last four decades can be explained as a local passive response to atmospheric forcing.

---

\* Current affiliation: Atmospheric and Environmental Research, Lexington, Massachusetts.

---

Corresponding author address: Martha Buckley, 131 Hartwell Avenue #4, Lexington, MA 02421.  
E-mail: marthab@alum.mit.edu

On the other hand, Bjerknes (1964) and Kushnir (1994) conclude that decadal SST anomalies are not forced by local atmospheric forcing, and thus the ocean must play an active role in setting SST on decadal time scales. Kushnir (1994) suggests that variability of the AMOC is a likely mechanism for creating the observed decadal SST anomalies.

The hypothesis that the AMOC may play a role in climate variability has prompted observational campaigns to monitor the AMOC and meridional OHT in the Atlantic. Data from the Rapid Climate Change (RAPID) and Meridional Overturning and Heatflux Array (MOCHA) observing systems, combined with wind stress estimates from satellites, has enabled the estimation of the AMOC and meridional OHT at 26.5°N since April 2004 (Cunningham et al. 2007; Johns et al. 2010). The success of the RAPID array and studies indicating that the AMOC is not coherent between the subtropical and subpolar gyres on interannual time scales (Bingham et al. 2007) have led to proposals for array-based observing systems at other latitudes, including the subpolar North Atlantic (OSNAP) and the South Atlantic at 34°S (SAMOC) (Lozier 2010). Additionally, several arrays in the western basin monitor the deep western boundary current (DWBC), including Line W off the coast of New England (Toole et al. 2011) and the Meridional Overturning Experiment (MOVE) array at 16°N (Kanzow et al. 2006). Unfortunately, time series of the AMOC at 26.5°N from the RAPID array are too short to estimate decadal AMOC variability and observations to access the meridional coherence of the AMOC are currently lacking.

The potential role of the AMOC in climate variability on decadal time scales and the inability of observations to firmly establish a connection owing to the paucity of long-term ocean observations have prompted numerous modeling studies. A plethora of models exhibit AMOC variability on decadal time scales and find decadal upper-ocean heat content (UOHC) anomalies associated with AMOC variability. Many of these studies argue that the UOHC anomalies are the result of OHT convergence anomalies associated with AMOC variability (Delworth et al. 1993; Delworth and Mann 2000; Knight et al. 2005; Zhang et al. 2007; Msadek and Frankignoul 2009). However, correlation does not imply causation, and, to our knowledge, none of these studies has explicitly shown that the observed UOHC anomalies are due to convergence of OHT anomalies resulting from changes in the AMOC. The observed correlations between UOHC anomalies and AMOC variability could simply be due to the thermal wind relation, which relates buoyancy anomalies on the boundaries to AMOC anomalies. Whether AMOC variability itself plays a role in creating

buoyancy anomalies on the boundaries or these anomalies are the result of other processes is not known.

In this paper we use coupled and ocean-only general circulation models (GCMs) run in idealized geometries to study the relationships between decadal AMOC and buoyancy variability. The models are slight modifications of the “Double Drake” setup described in Ferreira et al. (2010, hereafter FMC). As shown in FMC, the mean state of Double Drake bears an uncanny resemblance to the current climate, and we will show that the decadal variability seen in our models has features that resemble more complex models and the limited observations available. However, we do not intend to suggest that the models described here are realistic representations of the real ocean. Instead, our goal is to carefully examine the relationships between decadal buoyancy and AMOC variability, and determine if the AMOC plays an active role in setting SST on decadal time scales. To our knowledge no modeling study has unequivocally demonstrated the role of the AMOC (or the lack thereof) in setting SST on decadal time scales, despite the obvious importance of this question and the unique ability of model experiments to answer such a question. We are, of course, aware that our results may be model dependent, as is the case with all modeling experiments. As such, we present two different model setups. We find that despite the different character of MOC and buoyancy variability in the two models, the relationships between MOC variability and buoyancy anomalies are the same, suggesting the robustness of our main results.

In section 2 we describe the models used and their mean states. In section 3 we explore decadal MOC and buoyancy variability in our models. Decadal MOC variability is found to be related to changes in the buoyancy field along the western boundary according to the thermal wind relation. Buoyancy anomalies originate in the upper ocean of the subpolar gyre and upon reaching the western boundary, they are advected southward by the deep western boundary current, leading to latitudinally coherent MOC variability. In section 4, we address the origin of the decadal buoyancy anomalies, specifically the role of the MOC, atmospheric forcing, and baroclinic Rossby waves in creating the buoyancy anomalies. In section 5 we summarize the results of our modeling studies and hypothesize how our simple models might be used as a prism for understanding AMOC variability in more complex models and in nature.

## 2. Coupled aquaplanet model

### *a. Model setup*

The model used in this study is the Massachusetts Institute of Technology general circulation model (Marshall et al. 1997) run in a coupled atmosphere–ocean–sea ice

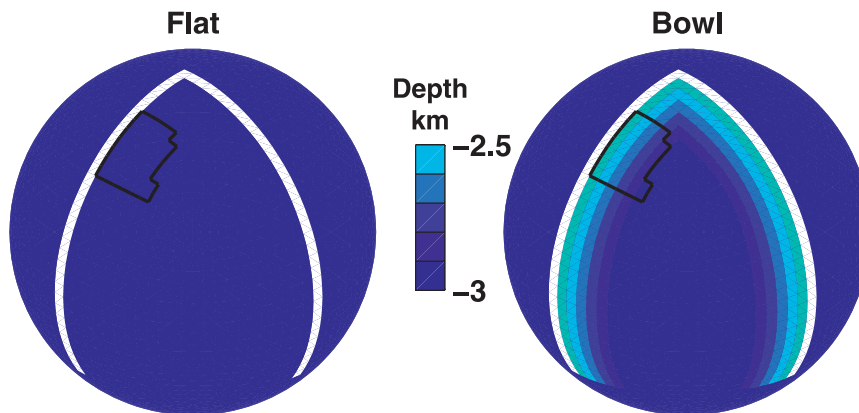


FIG. 1. Ocean geometry and depth (km) for (left) Flat and (right) Bowl. Two strips of land (white) extend from the north pole to  $34^{\circ}\text{S}$ , dividing the World Ocean into a small basin, a large basin, and a zonally unblocked southern ocean. In Flat the ocean has a constant depth of 3 km. In Bowl bathymetry is added to the small basin and the ocean depth varies from 3 km at the center of the basin to 2.5 km next to the meridional boundaries. The black boxes show the region along the western boundary of the subpolar gyre that is used to define the western boundary buoyancy (WBB) time series in section 3d.

setup. The model has realistic three-dimensional atmosphere and ocean dynamics, but it is run in idealized geometry. The planet is covered entirely by water except for two ridges that extend from the north pole to  $34^{\circ}\text{S}$ , dividing the ocean into a small basin (almost  $90^{\circ}$  wide), a large basin (almost  $270^{\circ}$  wide), and a zonally unblocked southern ocean. As described in FMC, this idealized Double Drake setup captures the gross features of the present-day ocean: a meridional asymmetry (circumpolar flow in the Southern Hemisphere and blocked flow in the Northern Hemisphere) and a zonal asymmetry (a small basin and a large basin).

The model setup is the same as is described in FMC. The atmosphere and ocean are integrated forward on the same cubed-sphere horizontal grid (Adcroft et al. 2004) at C24 (each face of the cube has  $24 \times 24$  grid points), yielding a resolution of  $3.7^{\circ}$  at the equator. The model uses the following (isomorphic) vertical coordinates: the rescaled pressure coordinate  $p^*$  for the atmosphere and the rescaled height coordinate  $z^*$  for the Boussinesq ocean (Adcroft and Campin 2004). The atmosphere is of “intermediate” complexity, employing the Simplified Parameterization, Primitive Equation Dynamics (SPEEDY) physics package described in Molteni (2003). The atmospheric model includes a four-band radiation scheme, a parameterization of moist convection, diagnostic clouds, and a boundary layer scheme. The atmospheric model has low vertical resolution and is composed of five vertical levels.

The ocean has a maximum depth of 3 km and has 15 vertical levels, increasing from a thickness of 30 m at the surface to 400 m at depth. As eddies are not resolved by

the low-resolution model, the effects of mesoscale eddies are parameterized as an advective process (Gent and McWilliams 1990) and an isopycnal diffusion (Redi 1982) with a transfer coefficient of  $1200 \text{ m}^2 \text{ s}^{-1}$  for both processes. Convective adjustment, implemented as an enhanced vertical mixing of temperature and salinity, is used to represent ocean convection (Klinger et al. 1996). The background vertical diffusivity is uniform and set to  $3 \times 10^{-5} \text{ m}^2 \text{ s}^{-1}$ .

Orbital forcing and  $\text{CO}_2$  levels are prescribed at present day values. The seasonal cycle is represented, but there is no diurnal cycle. Fluxes of momentum, heat, and freshwater are exchanged every hour (the ocean model time step). The model achieves perfect (machine accuracy) conservation of freshwater, heat, and salt during extended integrations, as discussed in Campin et al. (2008).

Motivated by the work of Winton (1997), who found that the presence of bottom topography substantially alters decadal variability in idealized, buoyancy-forced ocean-only models, we consider two types of bathymetry. In one setup, identical to the Double Drake model analyzed in FMC, the ocean has a uniform depth of 3 km (henceforth Flat). In the second setup bowl bathymetry is added to the small basin (henceforth Bowl) so that the ocean depth varies from 3 km at the center of the basin to 2.5 km next to the meridional boundaries (see Fig. 1). Each setup is initialized from rest with temperature and salinity from a January climatology of the equilibrium state discussed in FMC and run for 1000 years. To avoid the (short) adjustment period to the addition of bathymetry, only the last 800 years of these 1000-yr runs

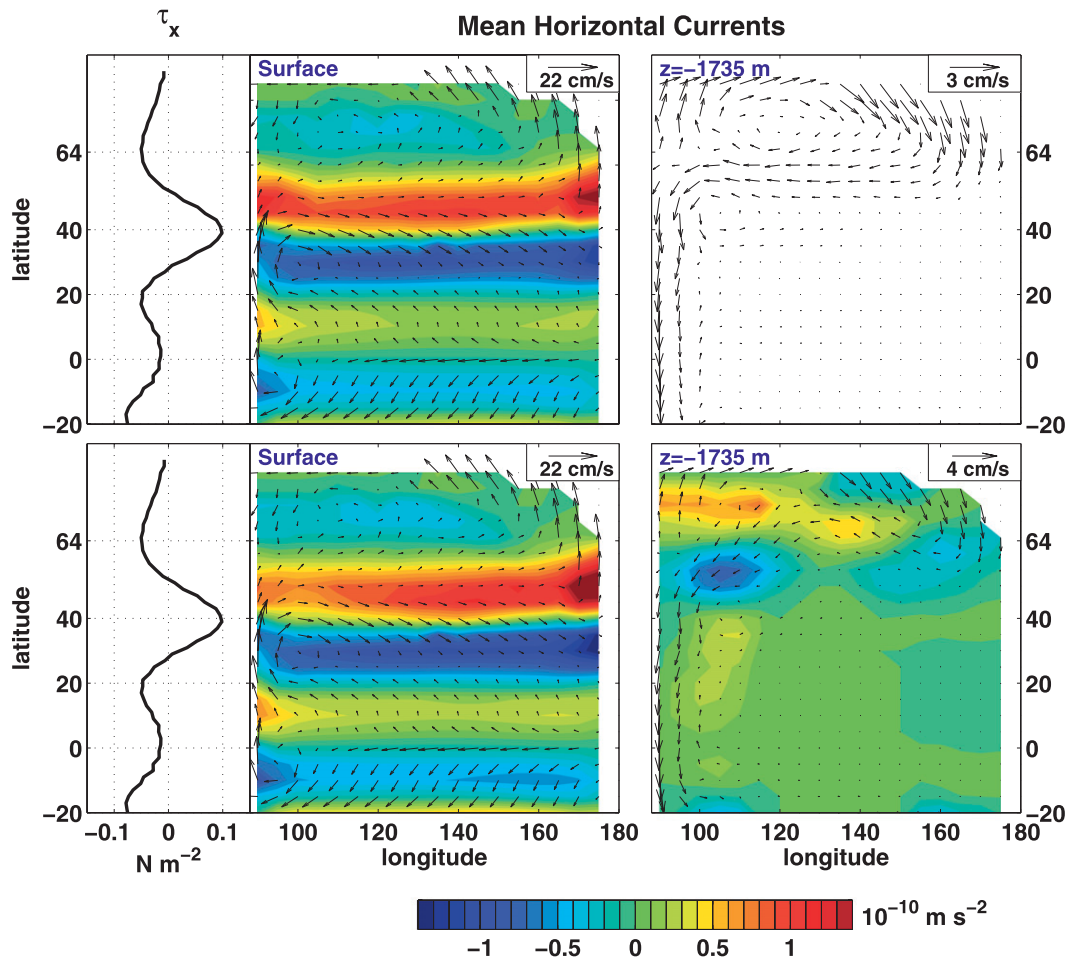


FIG. 2. (left) Average zonal-mean zonal wind stress in (top) Flat and (bottom) Bowl. (middle) Mean wind stress curl (colors) and horizontal currents at the surface (vectors) in the small basin for (top) Flat and (bottom) Bowl. (right) Mean bottom pressure torque (colors) and horizontal currents at a depth of 1735 m (vectors) for (top) Flat and (bottom) Bowl.

are analyzed. Since our interest is decadal variability, annual average outputs are analyzed.

#### b. Mean state

Here we briefly describe the very similar mean states of Flat and Bowl (see FMC for a detailed analysis of Flat, i.e., Double Drake). As discussed in FMC, the small basin is saltier than the large basin, similar to the higher salinity of the Atlantic relative to the Pacific. Although the higher sea surface salinity (SSS) in the small basin is partially compensated by warmer SST, the surface density is higher in the small basin than in the large basin. As a result, deep convection is restricted to the small basin (see Fig. 10 in FMC).

The zonal-mean zonal surface wind stress, shown in the left panels of Fig. 2, is easterly in the tropics, westerly in midlatitudes, and easterly near the poles. This large-scale pattern of wind stress forces the ocean's gyre circulations

and subtropical overturning cells. In steady state, neglecting friction, the vertically integrated vorticity equation is

$$\beta V = \frac{1}{\rho_o} \text{curl}_z \tau + \frac{1}{\rho_o} \text{curl}_z (p_b \nabla h), \quad (1)$$

where  $h(x, y)$  is the depth of the ocean,  $p_b$  is the bottom pressure, and  $\beta$  is the meridional gradient of the Coriolis parameter. The vertically integrated meridional velocity  $V$  is determined by two terms: the vertical component of the wind stress curl (first term on the right) and the bottom pressure torque (second term on the right). The colored contours in Fig. 2 show the windstress curl (middle panels) and bottom pressure torque (bottom-right panel) in the small basin. In Flat  $V$  is determined solely by the wind stress curl, leading to a barotropic streamfunction that is cyclonic in the subpolar gyre and anticyclonic in the subtropical gyres and "polar" gyre, the

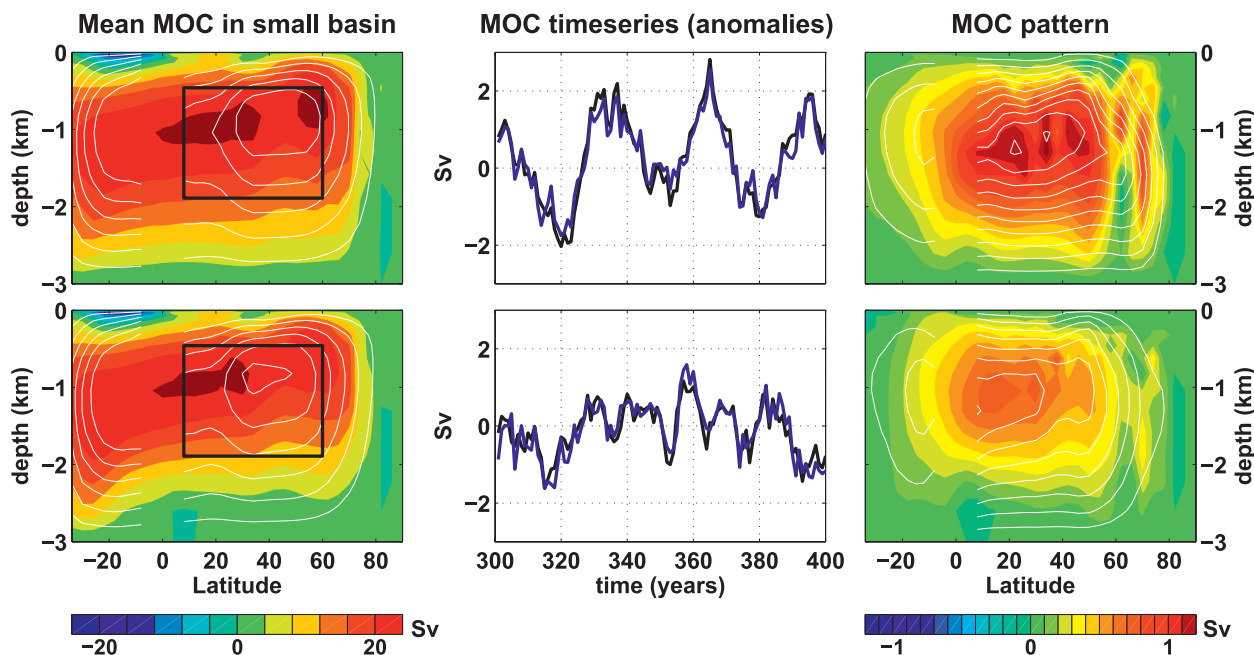


FIG. 3. (left) The residual mean MOC in the small basin (colors) and the MOC diagnosed from Eq. (5) (black/white contours) for (top) Flat and (bottom) Bowl. White (black) contours correspond to a positive (negative) MOC and the contour interval for both colors and black/white contours is 4 Sv. The black box shows the latitude and depth range ( $8^{\circ}$ – $60^{\circ}$ N, 460–1890-m depth) used to define the MOC time series. (middle) A 100-yr segment of anomalies of the yearly MOC time series (black) and reconstructed MOC time series [diagnosed from Eq. (5), blue] for (top) Flat and (bottom) Bowl. (right) The spatial patterns of MOC variability obtained by projecting MOC anomalies onto the MOC index (colors) and projecting MOC anomalies diagnosed from Eq. (5) onto the reconstructed MOC index (black/white contours) for (top) Flat and (bottom) Bowl. White (black) contours correspond to positive (negative) MOC anomalies and the contour interval for both the colors and black/white contours is 0.1 Sv.

region of negative wind stress curl north of  $64^{\circ}$ N. In Bowl the bottom pressure torque term is significant on the western boundary of the subpolar gyre and in the polar gyre. In the polar gyre the positive bottom pressure torque term is larger than the negative windstress curl, leading to a cyclonic barotropic streamfunction.

The vectors in Fig. 2 show the mean currents in the small basin at the surface (middle panels) and at a depth of 1735 m (right panels). The surface circulation is anticyclonic in the subtropical gyres and cyclonic in the subpolar gyre. At the surface the cyclonic subpolar gyre extends to the north pole in both Flat and Bowl. The strongest surface currents are found along the western boundary, except in the subpolar gyre where the strongest currents are along the eastern boundary. Deep-water formation in the small basin feeds a DWBC, which flows southward from  $64^{\circ}$ N to the exit of the small basin.

As a result of deep-water formation, a deep meridional overturning circulation develops in the small basin, similar to the overturning circulation in the present-day Atlantic Ocean. The residual-mean overturning streamfunction (the sum of the Eulerian and parameterized eddy-induced streamfunctions) in the small basin (henceforth called the MOC) in Flat and Bowl are plotted in the left panels

of Fig. 3.<sup>1</sup> The majority of the water that sinks in the small basin is still at depth when it exits the small basin, indicating that deep water upwells primarily in the southern ocean (and to a lesser extent in the large basin). In contrast, the MOC in the large basin (see Fig. 6 in FMC) is dominated by shallow wind-driven cells.

The meridional OHTs in the small and large basins of the model bear a striking similarity to those observed in the Atlantic and Indo-Pacific basins of the modern climate (see Fig. 2 in FMC). Like in the Indo-Pacific basin, the OHT in the large basin is due to the gyre circulations and Ekman transports and is poleward in both hemispheres. Similar to the Atlantic, the OHT transport in the small basin is northward in both hemispheres (see Fig. 4) because of the presence of a deep overturning cell.

In summary, the mean states of Flat and Bowl have many similarities to the present climate. Specifically, the small basin is saltier than the large basin and a deep,

<sup>1</sup> In Bowl bottom pressure torques potentially play a role in setting the pathways of the mean MOC, as discussed in a recent paper by Spence et al. (2012), although they found the effects to be largest in high-resolution models.

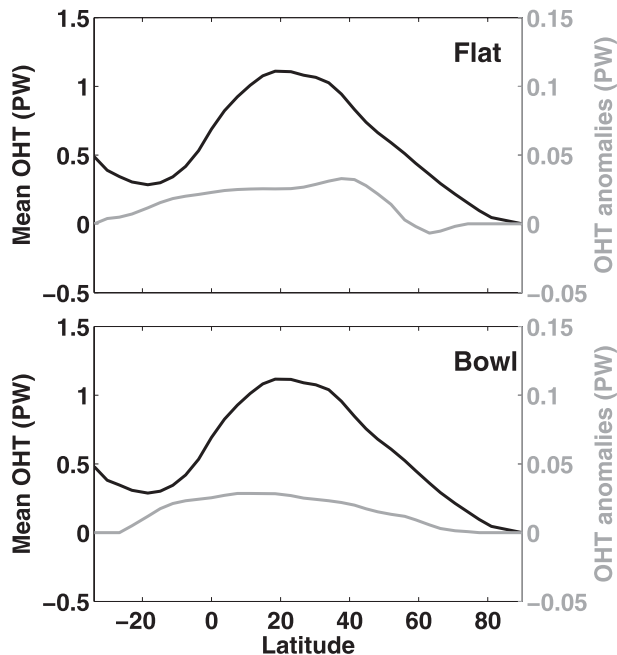


FIG. 4. Mean meridional ocean heat transport (OHT, black lines, left ordinate) and OHT anomalies associated with a positive MOC anomaly (gray lines, right ordinate) for (top) Flat and (bottom) Bowl. OHT anomalies associated with decadal MOC variability are computed by projecting OHT anomalies onto the MOC index at lag 0.

interhemispheric MOC develops in the small basin. Our focus is on the small basin, which can be thought of as an idealized Atlantic Ocean.

### 3. Decadal MOC and buoyancy variability

#### a. Decadal MOC variability

The MOC in the box from  $8^{\circ}$  to  $60^{\circ}\text{N}$ , 460 to 1890-m depth (box shown in black in left panels of Fig. 3) is used as a measure of the large-scale MOC variability. At each latitude, a yearly time series of the MOC is computed by taking the value of the MOC at the depth of the maximum of the mean MOC within the box. These time series are then averaged over all the latitudes in the box to create a MOC time series. The middle panels of Fig. 3 show 100-yr segments of yearly anomalies of the MOC time series for Flat (top) and the Bowl (bottom).

This definition of the MOC time series is chosen to focus our attention on large-scale (latitudinally coherent) MOC variability, and the analysis presented here is not sensitive to the box chosen. If instead a subtropical box spanning the equator ( $8^{\circ}\text{S}$ – $40^{\circ}\text{N}$ ) is chosen, variability of the resulting MOC time series (henceforth the subtropical MOC time series) is almost identical (correlation at lag 0 is 0.94 for Flat and 0.90 for Bowl). Thus, the low-frequency MOC variability seen in our model is coherent

between the subtropical and subpolar gyres and across the equator. On shorter (intraannual) time scales the MOC variability in the model does not exhibit such strong latitudinal coherence, as was noted by Bingham et al. (2007).

The right panels of Fig. 3 show the spatial patterns of MOC variability obtained by projecting MOC anomalies onto the normalized MOC time series (henceforth called the MOC index).<sup>2,3</sup> Each spatial pattern is interhemispheric and strongly resembles the first empirical orthogonal function (EOF) of the MOC (calculated over the latitude range  $20^{\circ}\text{S}$  to  $60^{\circ}\text{N}$ , not shown), which explains 54% of the variance for Flat and 40% of the variance for Bowl. The MOC time series is highly correlated with the first principle component (PC) time series of the MOC (correlation is 0.96 for Flat and 0.85 for Bowl), further confirming that the MOC time series captures the large-scale MOC variability.

The power spectrum of the MOC index in Flat (top-left panel of Fig. 5) is red at high frequencies, has a large peak at a period of about 34 yr, and flattens out at low frequencies. The power spectrum of the MOC index in Bowl (bottom-left panel of Fig. 5) is red at high frequencies and flattens out at low frequencies. The transition from a red spectrum to a flat spectrum occurs at a time scale of approximately 24 yr.

To examine the spatial and temporal variability of the MOC anomalies, the MOC index is projected onto MOC anomalies at various lags (see right panels of Figs. 6 and 7). Figure 8 (colors) shows MOC anomalies at the depth of the maximum of the mean MOC as a function of latitude and lag. In both Flat and Bowl, MOC anomalies originate in the subpolar gyre and travel southward with time.

Figure 4 shows the OHT anomalies that are associated with a positive MOC anomaly. OHT anomalies of 0.04 PW are associated with MOC anomalies with a standard deviation of 1 Sv ( $\text{Sv} \equiv 10^6 \text{ m}^3 \text{ s}^{-1}$ ). These OHT anomalies are in accord with decadal OHT anomalies observed in more realistic climate models. In the Hadley Centre Coupled Model, version 3 (HadCM3) decadal OHT anomalies of 0.04 PW are associated with MOC anomalies  $O(1 \text{ Sv})$  (Dong and Sutton 2001, 2003; Shaffrey and Sutton 2006). In the National Center for Atmospheric Research Community Climate System Model, version 3 (CCSM3) decadal OHT anomalies (amplitude of 0.12 PW) are associated with MOC anomalies with an amplitude of 4.5 Sv (Danabasoglu 2008).

<sup>2</sup> Projecting a data field onto a time series is equivalent to computing the covariance between the time series and the data field at each spatial location.

<sup>3</sup> A normalized time series has a mean of zero and standard deviation of one.

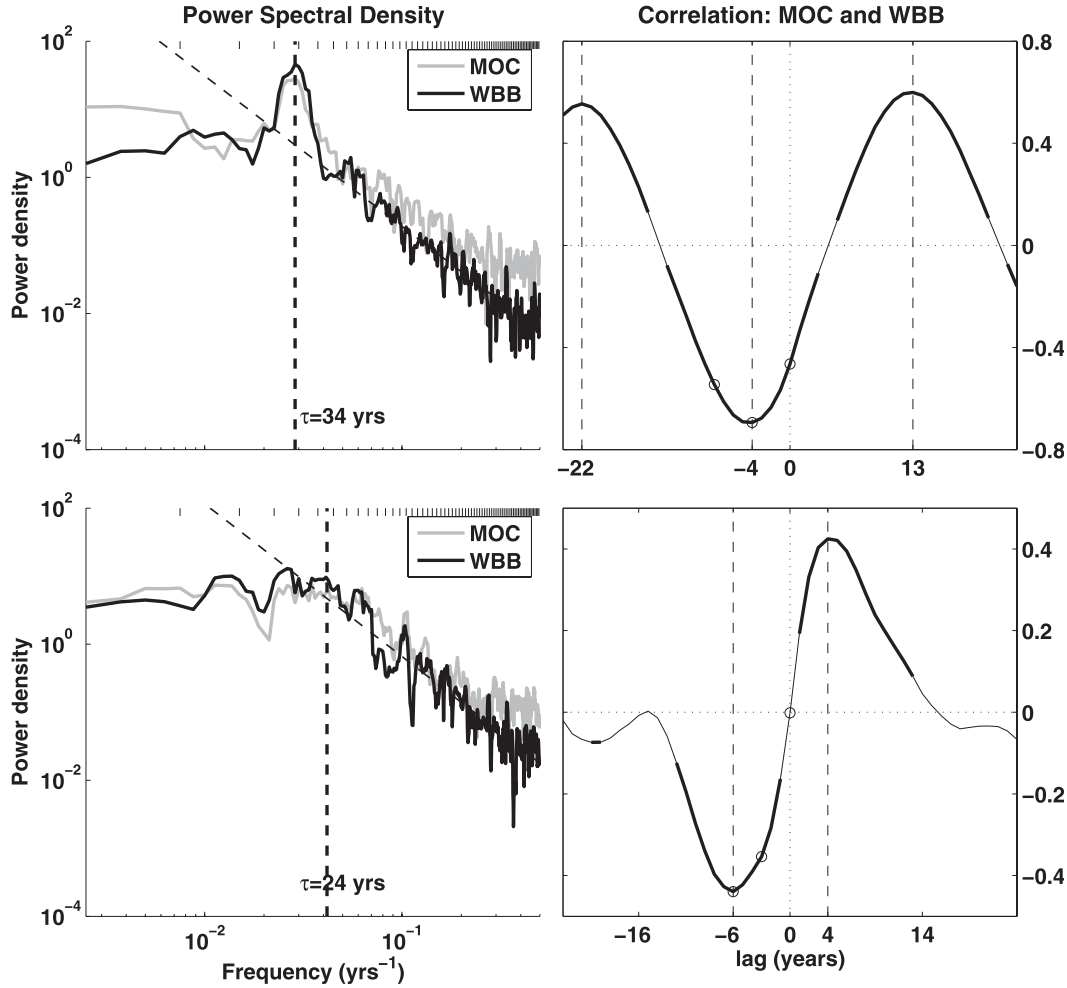


FIG. 5. (left) Power spectra  $P(f)$  of the MOC index (gray) and the WBB index (black) for (top) Flat and (bottom) Bowl. Dashed vertical lines indicate the time scale of the peak in Flat and the time scale at which the transition from a red spectrum to a flat spectrum occurs in Bowl. Dashed diagonal lines show a fit to the red portion ( $1/f < 24$  yr) of the spectrum of the WBB index:  $P(f) = Cf^{-\alpha}$ . We find  $\alpha = 2.21$  for Flat and  $\alpha = 2.24$  for Bowl. (right) Lagged correlation between MOC index and WBB index for (top) Flat and (bottom) Bowl. Lag = 0 corresponds to the maximum MOC index. Open circles indicate the lags for which spatial fields are plotted in Figs. 6 and 7.

### b. Diagnosis of MOC variability from thermal wind relation and Ekman transports

To examine the origin of the MOC variability observed in the model, we decompose the meridional velocity  $v$  into geostrophic and Ekman components (Lee and Marotzke 1998; Hirschi and Marotzke 2007):  $v = v_g + v_{\text{Ek}}$ . The geostrophic velocity  $v_g$  is calculated from the buoyancy field  $b$  using the vertically integrated thermal wind relation:

$$v_g(z) = \frac{1}{f} \int_{-h}^z \frac{\partial b}{\partial x} dz + v_b, \quad (2)$$

in which  $f$  is the Coriolis parameter,  $h(x, y)$  is the ocean depth, and  $v_b$  is the unknown meridional bottom

velocity. The Ekman velocity  $v_{\text{Ek}}$  is related to the zonal surface windstress  $\tau^x$  as

$$v_{\text{Ek}} = -\frac{\tau^x}{\rho_o f \delta z} \quad (3)$$

in which  $\rho_o$  is a reference density and  $\delta z$  is the thickness of the Ekman layer (or top model layer). The mass conservation constraint can be used to solve for the zonal-average bottom velocity  $\bar{v}_b$ . We find

$$\bar{v}_b = -\frac{1}{A} \int_{x_w}^{x_e} dx \int_{-h}^0 \left( \frac{1}{f} \int_{-h}^z \frac{\partial b}{\partial x} dz + v_{\text{Ek}} \right) dz, \quad (4)$$

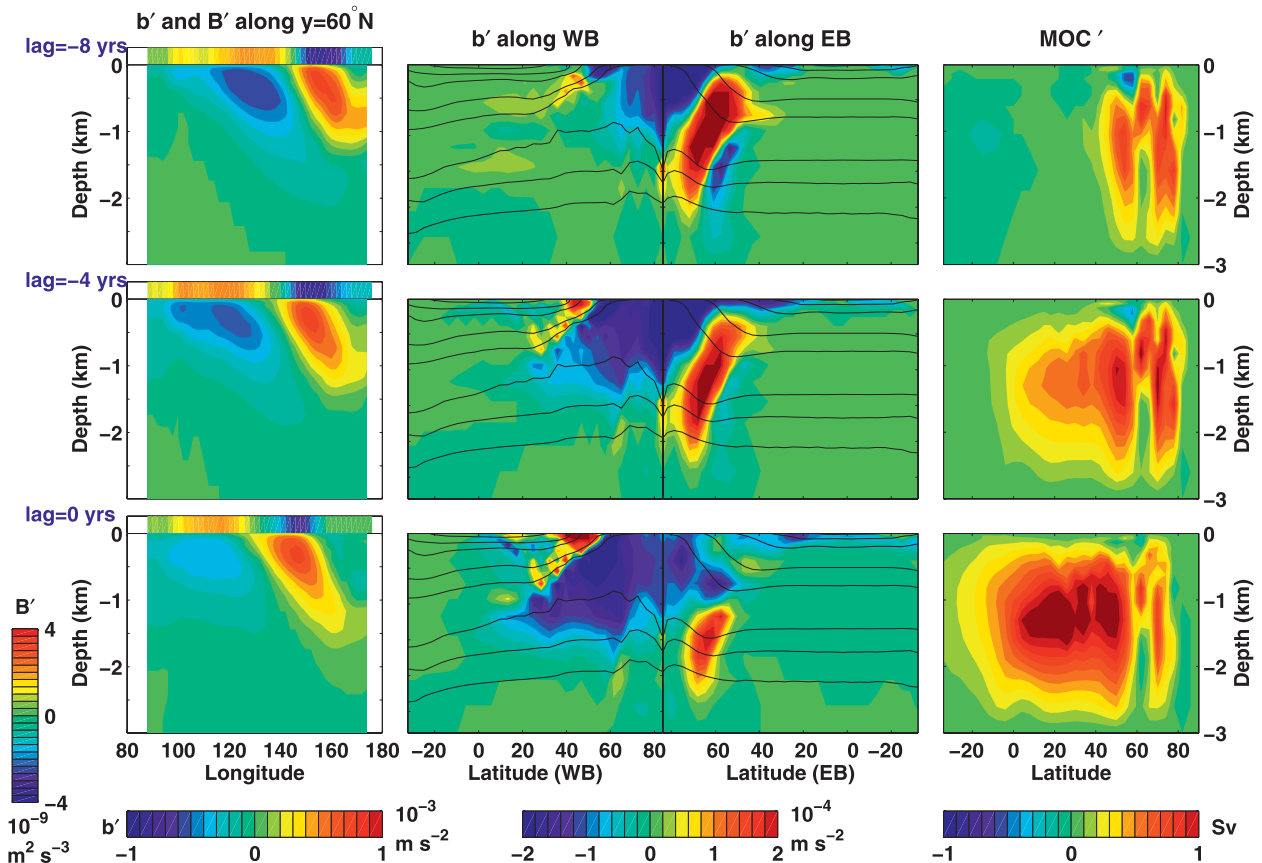


FIG. 6. Flat: (left) east-west sections of buoyancy and air-sea buoyancy flux anomalies at  $60^{\circ}\text{N}$ , (middle) buoyancy anomalies along the western and eastern boundaries of the small basin, and (right) MOC anomalies projected onto the MOC index at various lags. Buoyancy and MOC anomalies are shown for (top) lag =  $-8$  yr, (middle) lag =  $-4$  yr, and (bottom) lag =  $0$  yr. Air-sea buoyancy flux anomalies are shown one year earlier to demonstrate that air-sea buoyancy fluxes damp the decadal buoyancy anomalies. Only covariances significant at the 95% confidence level are plotted. The thin black lines in the middle panels show the mean isopycnals along the western and eastern boundaries.

where  $A$  is the area of the longitude–depth section. A streamfunction can then be computed by integrating  $v$  zonally and vertically:

$$\tilde{\Psi}(z) = \int_{x_w}^{x_e} dx \int_{-h}^z v dz. \quad (5)$$

The left panels of Fig. 3 (contours) show the mean MOC diagnosed according to Eq. (5). The spatial correlation between the mean Eulerian<sup>4</sup> MOC and the MOC estimate is 0.81 for Flat and 0.82 for Bowl. Errors are largely due to errors in determining the barotropic flow, but the neglect of friction and nonlinearity also

play a role.<sup>5</sup> The center panels of Fig. 3 compare the variability of the actual MOC time series (MOC in the box from  $8^{\circ}$  to  $60^{\circ}\text{N}$ , 460 to 1890-m depth) to the variability of the reconstructed MOC time series [MOC in same box, but when the MOC is calculated from Eq. (5)]. Despite the errors in diagnosing the mean MOC, MOC variability in the reconstruction matches the actual MOC variability almost exactly (correlation is 0.95 for Flat and 0.90 for Bowl).

The right panels of Fig. 3 (contours) show the spatial patterns of MOC variability obtained by projecting the reconstructed MOC anomalies onto the normalized

<sup>4</sup> When computing spatial correlations, we compare the reconstructed MOC to the Eulerian MOC rather than the residual MOC since the bolus part cannot be estimated from the thermal wind relation. However, in the small basin, the mean Eulerian and residual MOC are very similar (spatial correlation is 0.98 for Flat and 0.97 for Bowl).

<sup>5</sup> If we instead diagnose the MOC from the pressure field, which does not require us to estimate the barotropic flow from mass conservation, the MOC estimate improves markedly. The spatial correlation between the mean MOC and the MOC estimate improves to 0.96 for both Flat and Bowl. Additionally, the vertical structure of the MOC, including the subtropical cells, is properly represented.



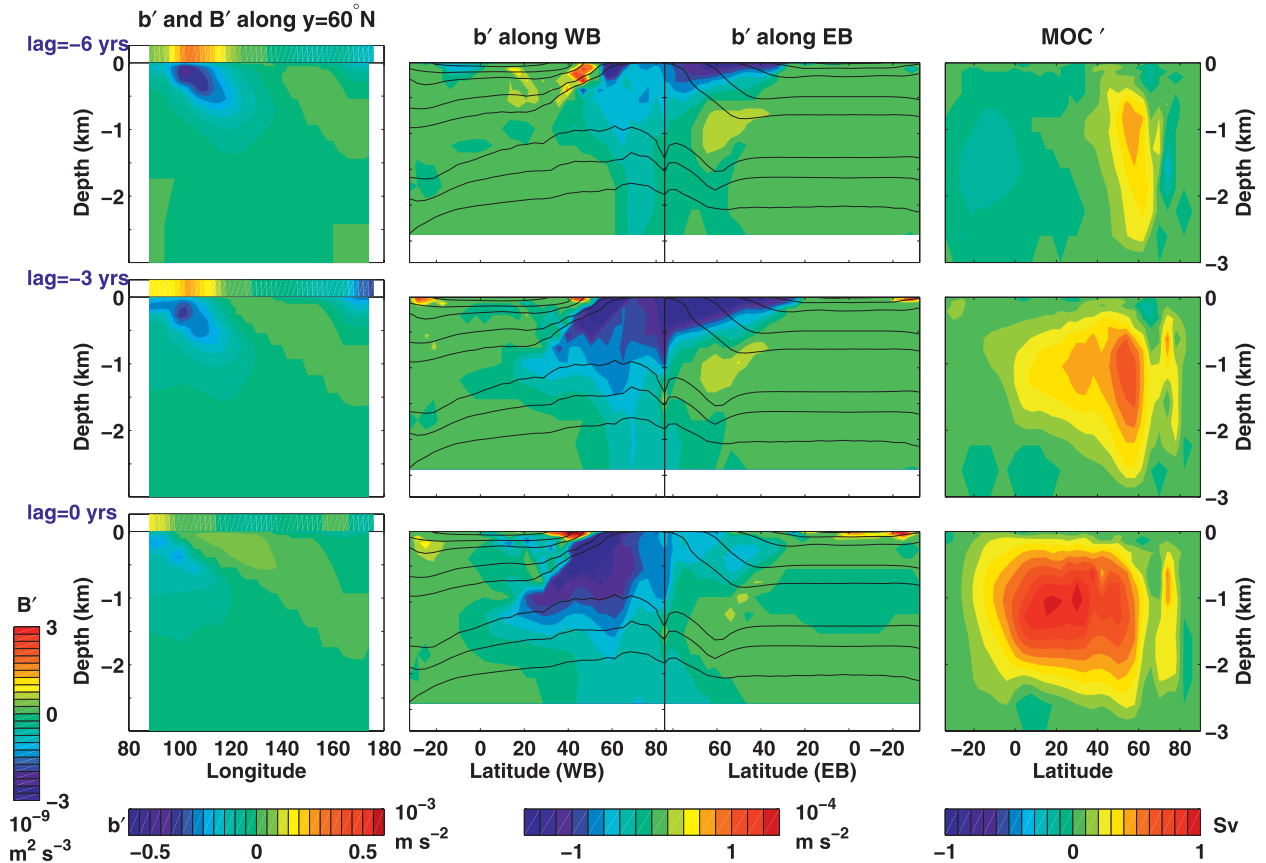


FIG. 7. Bowl: As in Fig. 6 but for Bowl and buoyancy and MOC anomalies are shown for (top) lag = -6 yr, (middle) lag = -3 yr, and (bottom) lag = 0 yr.

reconstructed MOC time series (henceforth called the reconstructed MOC index). The spatial correlation between the reconstructed MOC variability and the actual MOC variability is 0.97 for Flat and 0.92 for Bowl. The spatial and temporal variability of the MOC and the reconstructed MOC are compared in Fig. 8, which shows MOC anomalies at the depth of the maximum of the mean MOC as a function of latitude and lag. The reconstructed MOC variability (contours) matches the actual decadal MOC anomalies (colors) almost exactly except in the high northern latitudes. The calculation is less accurate in the high northern latitudes owing to the small number of grid points in the northern apex of the small basin. Additionally, the flow may not be geostrophic near the boundaries due to the friction and inertial effects.

In summary, while there are substantial errors in estimating the mean MOC from Eq. (5), it is an extremely accurate method for diagnosing MOC variability, a fact which has been noted by other studies (Hirschi and Marotzke 2007). The primary reason for the errors in the mean MOC is that the barotropic flow is difficult to estimate in regions where bottom velocities are not small

(Baehr et al. 2004). However, although bottom velocities are often not small, their variability on decadal time scales tends to be quite small, so errors in estimating the barotropic flow do not affect our estimates of MOC variability.

#### 1) ROLE OF GEOSTROPHIC AND EKMAN TRANSPORTS

To examine the relative contributions of geostrophic and ageostrophic (Ekman) velocities to decadal MOC variability, we calculate  $\Psi'_{tw}$ , the decadal MOC anomalies expected from the thermal wind contribution alone (setting  $v'_{Ek} = 0$ ). The streamfunction  $\Psi'_{tw}$  is indistinguishable from  $\Psi'$  (not shown), demonstrating that decadal MOC anomalies are related to buoyancy anomalies on the boundaries according to the thermal wind relation, and ageostrophic MOC anomalies due to Ekman transport variability are negligible on decadal time scales. Our results are in accord with previous modeling studies (Sime et al. 2006; Hirschi and Marotzke 2007; Hirschi et al. 2007) and analyses of ocean state estimates (Cabanès et al. 2008), which found that Ekman transport variability plays a role in AMOC variability on short time scales,

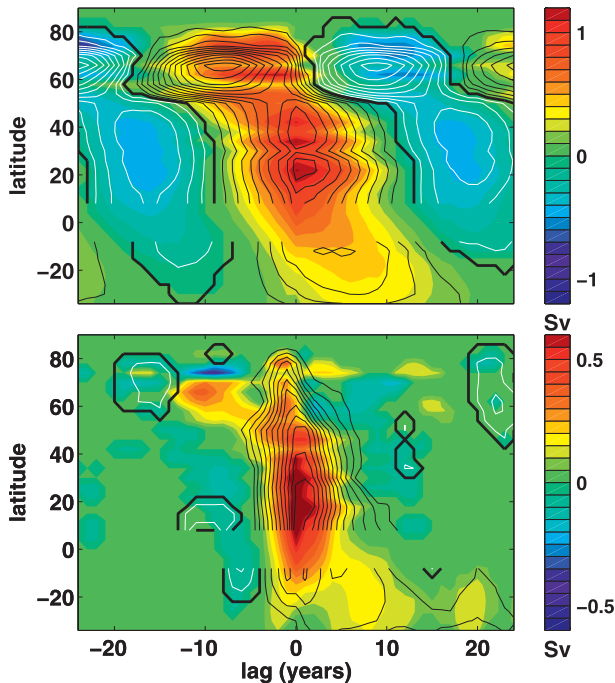


FIG. 8. MOC anomalies at the depth of the maximum of the mean MOC (below 460 m) as a function of latitude and lag for (top) Flat and (bottom) Bowl. Colors show the actual MOC anomalies and contours show MOC anomalies calculated from buoyancy and windstress fields according to Eq. (5). Black (white) contours indicate positive (negative) MOC anomalies. The contour interval is 0.1 Sv for Flat and 0.05 Sv for Bowl for both the colors and black/white contours.

while AMOC variability on longer (interannual to decadal) time scales is primarily related to changes in the density field.

## 2) ROLE OF WESTERN AND EASTERN BOUNDARIES

To examine the relative roles of buoyancy anomalies at the western and eastern boundaries in contributing to MOC variability, we project buoyancy anomalies on the western and eastern boundaries onto the MOC index at various lags (see middle panels of Figs. 6 and 7). In the subpolar gyre both the eastern and western boundaries play a role in MOC variability in Flat, whereas only the contribution of the western boundary is important in Bowl. Outside the subpolar gyre MOC anomalies in both Flat and Bowl are due to buoyancy anomalies on the western boundary. Prior to the maximum MOC anomaly, a negative buoyancy anomaly reaches the western boundary of the subpolar gyre. The buoyancy anomaly travels southward following the mean isopycnals, leading to latitudinally coherent MOC variability. Because of the slow travel of the buoyancy anomalies down the western boundary (approximately  $2 \text{ cm s}^{-1}$ ) and their

path along the mean isopycnals, we hypothesize that the anomalies are advected southward by the DWBC. The advective nature of the travel of buoyancy anomalies is in accord with observational results tracking potential vorticity anomalies (Curry et al. 1998; Peña-Molino et al. 2011) and several modeling studies (Marotzke and Klinger 2000; Zhang 2010), but in contrast to numerous theoretical studies that implicate Kelvin waves in the southward communication of AMOC variability (Kawase 1987; Johnson and Marshall 2002a,b; Deshayes and Frankignoul 2005).

### c. Summary

In summary, our model exhibits large-scale, latitudinally coherent MOC variability on decadal time scales. Decadal MOC anomalies are related to buoyancy anomalies on the boundaries in accord with the thermal wind relation. Outside the subpolar gyre anomalies on the eastern boundary are negligible, and thus MOC variability is determined solely by buoyancy anomalies on the western boundary. Western boundary buoyancy anomalies are first seen in the subpolar gyre and subsequently travel southward along the western boundary, following the mean isopycnals.

### d. Decadal buoyancy anomalies

Projecting subsurface buoyancy anomalies onto the MOC index at various lags demonstrates that upper-ocean buoyancy anomalies in the subpolar gyre are associated with decadal MOC variability. The left panels of Figs. 6 and 7 show buoyancy and air–sea buoyancy flux anomalies through  $60^\circ\text{N}$  (the latitude of the maximum buoyancy anomalies) projected onto the MOC index at various lags. The buoyancy anomalies, which are  $O(10^{-3} \text{ m s}^{-2})$  near the surface and decay with depth, are dominated by temperature anomalies ( $0.8^\circ\text{C}$  in Flat,  $0.5^\circ\text{C}$  in Bowl) and associated with smaller compensating salinity anomalies ( $0.065 \text{ psu}$  in Flat,  $0.036 \text{ psu}$  in Bowl). In Flat buoyancy anomalies originate along the eastern boundary and propagate westward. In Bowl buoyancy anomalies appear to originate in the interior of the gyre near the western boundary. When these buoyancy anomalies strike the western boundary, they are advected southward by the DWBC, resulting in MOC variability in thermal wind balance with the buoyancy anomalies on the boundary, as described in section 3b.

The importance of buoyancy anomalies on the western boundary to MOC variability led us to define a time series of western boundary buoyancy. Annual-mean buoyancy anomalies are averaged over a box along the western boundary between  $40^\circ$  and  $65^\circ\text{N}$  latitude (box shown in black in Fig. 1) from 130- to 320-m depth to compute a western boundary buoyancy (WBB) time series. One-hundred-year segments of the WBB time

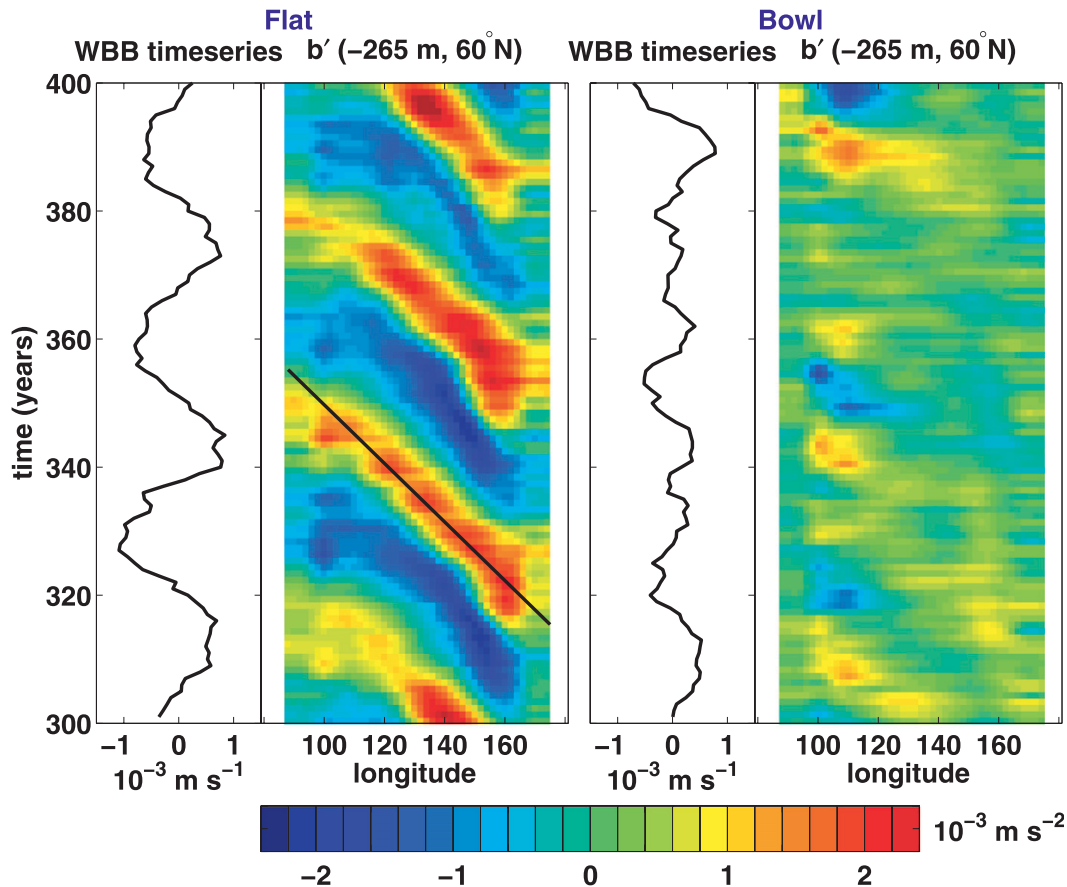


FIG. 9. Plot of the WBB time series (black curves) and Hovmöller plot of subsurface (depth 265 m) buoyancy anomalies averaged over the latitude range  $55^{\circ}$ – $65^{\circ}$ N (colors) for (left) Flat and (right) Bowl. Black lines on Hovmöller plot for Flat show an estimate of the westward phase velocity of the buoyancy anomalies.

series are plotted in black in Fig. 9. The power spectra of the normalized WBB time series (henceforth the WBB index) are plotted in the left panels Fig. 5. In both Flat and Bowl, the power spectrum of the WBB index is very similar to the power spectrum of the MOC index. The right panels of Fig. 5 show the lagged correlation between the MOC index and the WBB index. Negative buoyancy anomalies on the western boundary precede the maximum MOC anomaly by 4 yr in Flat and 6 yr in Bowl.

#### 4. Origin of buoyancy anomalies

Our analysis thus far has demonstrated that decadal MOC anomalies are related to buoyancy anomalies that originate in the subpolar gyre. In this section we explain the origin of the buoyancy anomalies in the subpolar gyre.

##### a. Role of air–sea heat fluxes

The left panels of Figs. 6 and 7 show buoyancy and air–sea buoyancy flux anomalies through  $60^{\circ}$ N (the latitude

of the maximum buoyancy anomalies) projected onto the MOC index at various lags. Air–sea buoyancy fluxes  $O(4 \times 10^{-9} \text{ m}^2 \text{ s}^{-3})$  are associated with decadal buoyancy anomalies  $O(10^{-3} \text{ m s}^{-2})$ . The buoyancy fluxes are dominated by heat fluxes, which have a maximum magnitude of  $8 \text{ W m}^{-2}$  in Flat and  $6 \text{ W m}^{-2}$  in Bowl. Air–sea buoyancy fluxes damp the buoyancy anomalies at all stages of the evolution of the buoyancy anomalies. Previous observational (Deser and Blackmon 1993; Kushnir 1994; Dong and Kelly 2004; Dong et al. 2007) and modeling (Dong and Sutton 2003; Shaffrey and Sutton 2006; Grist et al. 2010) studies also found that on short time scales upper-ocean temperature anomalies are forced by air–sea heat fluxes, while on long time scales the ocean circulation plays a role in creating temperature anomalies, which are then damped by air–sea heat fluxes.

##### b. Role of the MOC in creating decadal buoyancy anomalies

In this section we will address whether the MOC plays an active role in creating decadal buoyancy anomalies in

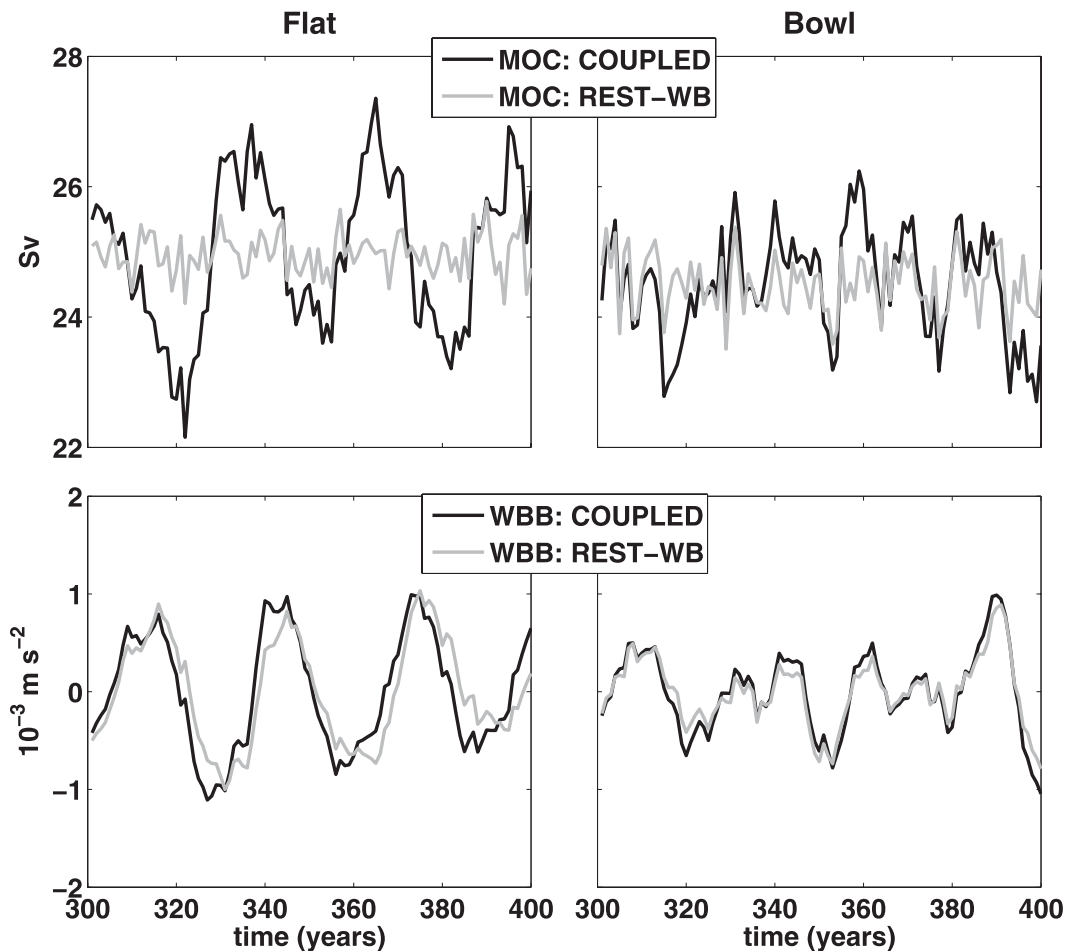


FIG. 10. (top) Yearly subtropical MOC time series in the coupled model (black curve) and ocean-only model experiment RESTORE-WB (gray curve) and (bottom) WBB time series in the coupled model (black curve) and RESTORE-WB (gray curve): (left) Flat and (right) Bowl.

the subpolar gyre. We conduct an ocean-only experiment in which we suppress variability of the large-scale MOC and determine if buoyancy anomalies in the subpolar gyre are altered. The ocean model is initialized with a state from the spunup coupled model and forced with 5-day mean time series of heat, freshwater, and momentum fluxes from the coupled model as well as restoring of SST and SSS to that of the coupled run on time scales of 71 days and 1 year, respectively.<sup>6</sup> Along the western boundary south of 50°N temperature and

salinity are restored to climatology throughout the water column with a restoring time scale of two months. This restoring at depth suppresses the large-scale MOC variability since the MOC is concentrated on the western boundary but does not directly alter temperature and salinity in the subpolar gyre where the buoyancy anomalies originate. This experiment will be referred to as RESTORE-WB.

The top panels of Fig. 10 show the subtropical MOC time series for the coupled run and the RESTORE-WB experiment. We chose a box (8°S–40°N, 460–1890-m depth) that excludes the subpolar gyre to define our MOC time series since we are interested in understanding if MOC anomalies outside the subpolar gyre play a role in creating the buoyancy anomalies in the subpolar gyre. Restoring temperature and salinity along the western boundary greatly reduces the amplitude of subtropical MOC variability in both Flat and Bowl. The modest MOC variability observed in the RESTORE-WB

<sup>6</sup> Restoring of SST and SSS is needed for the ocean-only model to accurately reproduce the coupled model trajectory since a number of nonlinear processes, such as convective events, are not well represented when the ocean model is forced with 5-day averaged forcing. If no restoring is included, the ocean-only model trajectory slowly diverges from that of the coupled model. These differences substantially affect the MOC and WBB time series after approximately 70 years.

experiment is primarily due to variability in Ekman transport forced by wind variability (not shown). The bottom panels of Fig. 10 show buoyancy anomalies averaged over a box near the western boundary of the subpolar gyre.<sup>7</sup> Although MOC variability has been suppressed substantially, the buoyancy anomalies near the western boundary of the subpolar gyre remain virtually unchanged.

From this experiment we conclude that although large-scale MOC variability does lead to OHT anomalies (see Fig. 4), these transports are not responsible for creating the buoyancy anomalies in the subpolar gyre that drive the MOC variability. In both Flat and Bowl the large-scale MOC responds passively to buoyancy anomalies that originate in the subpolar gyre. Of course variability of the velocity field (and hence the MOC) and buoyancy field in the subpolar gyre are tightly coupled according to the thermal wind relation. The point here is that variability of the large-scale MOC (outside the subpolar gyre) and the resulting OHT anomalies do not play a role in creating the buoyancy anomalies seen in the subpolar gyre. These anomalies are formed by processes local to the subpolar gyre. Thus, if we can explain the origin of these buoyancy anomalies, we will successfully explain the mode of MOC variability.

### c. Role of atmospheric forcing

To determine if stochastic atmospheric forcing is needed to excite buoyancy and MOC variability, we conduct an ocean-only experiment in which the ocean is forced with climatological forcing. In the experiment, which we will refer to as CLIM-DAMP, the ocean model is forced with 5-day climatological (100-yr average from coupled model) forcing of heat, momentum, and freshwater and damping of SST to climatology with the canonical value of  $20 \text{ W m}^{-2} \text{ K}^{-1}$  (Frankignoul et al. 1998).

The MOC time series from CLIM-DAMP is compared to the MOC time series from the coupled run in Fig. 11. For Flat CLIM-DAMP reproduces the low-frequency MOC variability of the coupled model amazingly well. If realistic damping is not included in the ocean-only experiment, the decadal MOC variability is much larger than in the coupled model (not shown). Thus, the decadal mode of variability observed in Flat is a self-sustained ocean-only mode damped by air-sea heat fluxes. For Bowl MOC variability rapidly decays in CLIM-DAMP. In the presence of realistic damping by air-sea heat

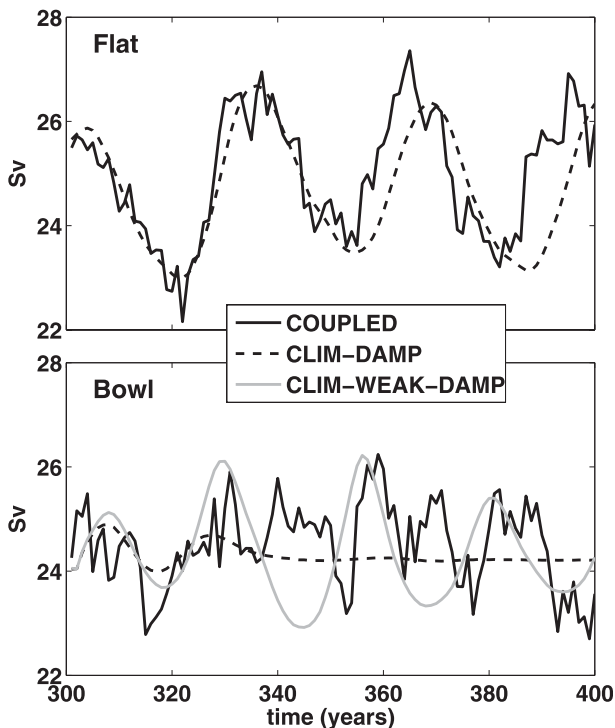


FIG. 11. Yearly subtropical MOC time series in the coupled model (solid black curve) and ocean-only model experiment CLIM-DAMP (dashed black curve) for (top) Flat and (bottom) Bowl. For Bowl an additional experiment, CLIM-WEAK-DAMP is shown (gray curve). CLIM-WEAK-DAMP is the same as CLIM-DAMP, but the damping of SST anomalies is set to be  $4 \text{ W m}^{-2} \text{ K}^{-1}$  rather than the canonical value of  $20 \text{ W m}^{-2} \text{ K}^{-1}$ .

fluxes, decadal MOC and buoyancy variability does not exist without continuous excitation by stochastic atmospheric forcing.

An additional experiment CLIM-WEAK-DAMP in which damping of SST anomalies was set to be only  $4 \text{ W m}^{-2} \text{ K}^{-1}$  demonstrates that if damping of SST anomalies is weak enough, MOC variability persists in Bowl even in the absence of stochastic atmospheric forcing. Although the MOC variability observed in Bowl in the CLIM-WEAK-DAMP experiment is quite regular, like that of the experiment CLIM-DAMP in Flat, the spatial pattern of the buoyancy variability in CLIM-WEAK-DAMP is very different to that observed in Flat. The buoyancy variability in Bowl in both CLIM-WEAK-DAMP and the coupled model is maximal near the western boundary of the subpolar gyre. In contrast, in Flat buoyancy anomalies originate near the eastern boundary and propagate westward in both the CLIM-DAMP experiment and the coupled model. Thus, adding bathymetry has not merely increased dissipation, leading to damped rather than self-sustained modes, it has fundamentally altered the character of the variability.

<sup>7</sup> The box is the same as shown in Fig. 1 ( $40^{\circ}\text{N}$  and  $65^{\circ}\text{N}$ , 130–320-m depth), but the points immediately adjacent to the western boundary have been removed since temperature and salinity are restored to climatology along the western boundary.

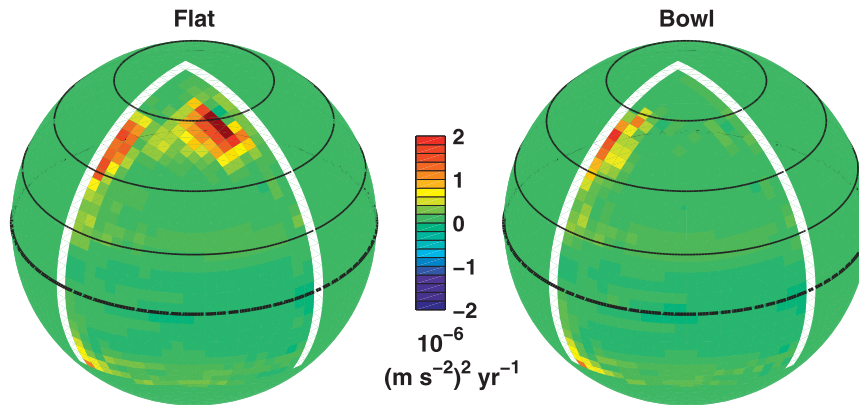


FIG. 12. The production of buoyancy variance  $-\overline{\mathbf{u}'b'} \cdot \nabla \bar{b}$  in (left) Flat and (right) Bowl. Thick black line is at the equator and thin black lines show the lines of zero windstress curl in the Northern Hemisphere ( $20^\circ$ ,  $40^\circ$ , and  $64^\circ\text{N}$ ).

Additional ocean-only experiments (not shown) demonstrate that in Bowl both stochastic wind and buoyancy forcing are capable of exciting the mode of buoyancy and MOC variability. Thus, we conclude that the decadal buoyancy and MOC variability in Bowl is due to damped ocean-only mode(s) excited by stochastic atmospheric forcing.

#### d. Creation of buoyancy variance

In this section we will show that decadal buoyancy anomalies extract energy out of the mean flow, which allows them to grow. Taking the time mean (denoted by overbars) of the linearized buoyancy variance equation, one can show that, in order for a mode to grow against mixing and damping by air–sea buoyancy fluxes, the term  $-\overline{\mathbf{u}'b'} \cdot \nabla \bar{b}$  must be positive averaged over the domain (Colin de Verdière and Huck 1999). Here  $\bar{\mathbf{u}}$  and  $\bar{b}$  are the mean velocity and buoyancy fields and  $\mathbf{u}'$  and  $b'$  are the deviations from the time mean fields.<sup>8</sup>

In Flat  $-\overline{\mathbf{u}'b'} \cdot \nabla \bar{b} > 0$  in a broad region near the eastern boundary and also along the western boundary of the subpolar gyre (see left panel of Fig. 12). In Bowl  $-\overline{\mathbf{u}'b'} \cdot \nabla \bar{b} > 0$  only along the western boundary of the subpolar gyre (see right panel of Fig. 12). In both models the domain average of  $-\overline{\mathbf{u}'b'} \cdot \nabla \bar{b} > 0$ , indicating that perturbations can grow by extracting

energy from the mean flow. Unfortunately, it is more difficult to conclude where in the domain the perturbations are actually extracting energy from the mean flow. Locally,  $-\overline{\mathbf{u}'b'} \cdot \nabla \bar{b} > 0$  can mean either that perturbations are extracting energy from the mean flow locally or that waves are transporting variance to that location.

#### e. Propagation of buoyancy anomalies

Hovmöller plots of yearly subsurface buoyancy anomalies averaged over the latitude range  $55^\circ$ – $65^\circ\text{N}$ , the latitude range of the maximum buoyancy anomalies, are shown as a function of longitude and time in Fig. 9. In Flat buoyancy anomalies originate near the eastern boundary and propagate westward, taking approximately 34 years to cross the basin (average velocity of  $-0.47 \text{ cm s}^{-1}$ ). Buoyancy anomalies move slower  $c \approx -0.35 \text{ cm s}^{-1}$  in the eastern part of the basin and speed up to  $c \approx -0.87 \text{ cm s}^{-1}$  as they approach the western boundary. While there is some evidence of westward propagation in Bowl, the largest buoyancy anomalies are confined to the region near the western boundary. The ubiquity of westward propagation led us to ask if the buoyancy variability in the model can be explained by a Rossby wave model. A number of studies have previously shown that Rossby wave models forced by windstress anomalies successfully capture much of the observed sea surface height and thermocline depth variability measured by tide gauges (Sturges and Hong 1995), hydrographic data (Sturges et al. 1998; Schneider and Miller 2001), and satellite altimetry (Fu and Qui 2002; Qiu 2002; Qiu and Chen 2006). Details of the Rossby wave model are described in the appendix.

The left panels of Fig. 13 show baroclinic pressure potential anomalies  $p'_{bc}$  (pressure potential anomalies

<sup>8</sup> We avoid the terminology “eddy” creation of buoyancy variance, used by Colin de Verdière and Huck (1999), since in our coarse resolution model eddies are not resolved. In parameterizing the eddies it is assumed that the eddy buoyancy flux ( $\mathbf{u}^*b^*$ ) is down the mean buoyancy gradient:  $-\overline{\mathbf{u}^*b^*} = -K_e \nabla \bar{b}$ , where  $K_e$  is the eddy diffusivity. Therefore, the effect of the parameterized eddies (which was not included in our calculation)  $-\overline{\mathbf{u}^*b^*} \cdot \nabla \bar{b} > 0$  everywhere.

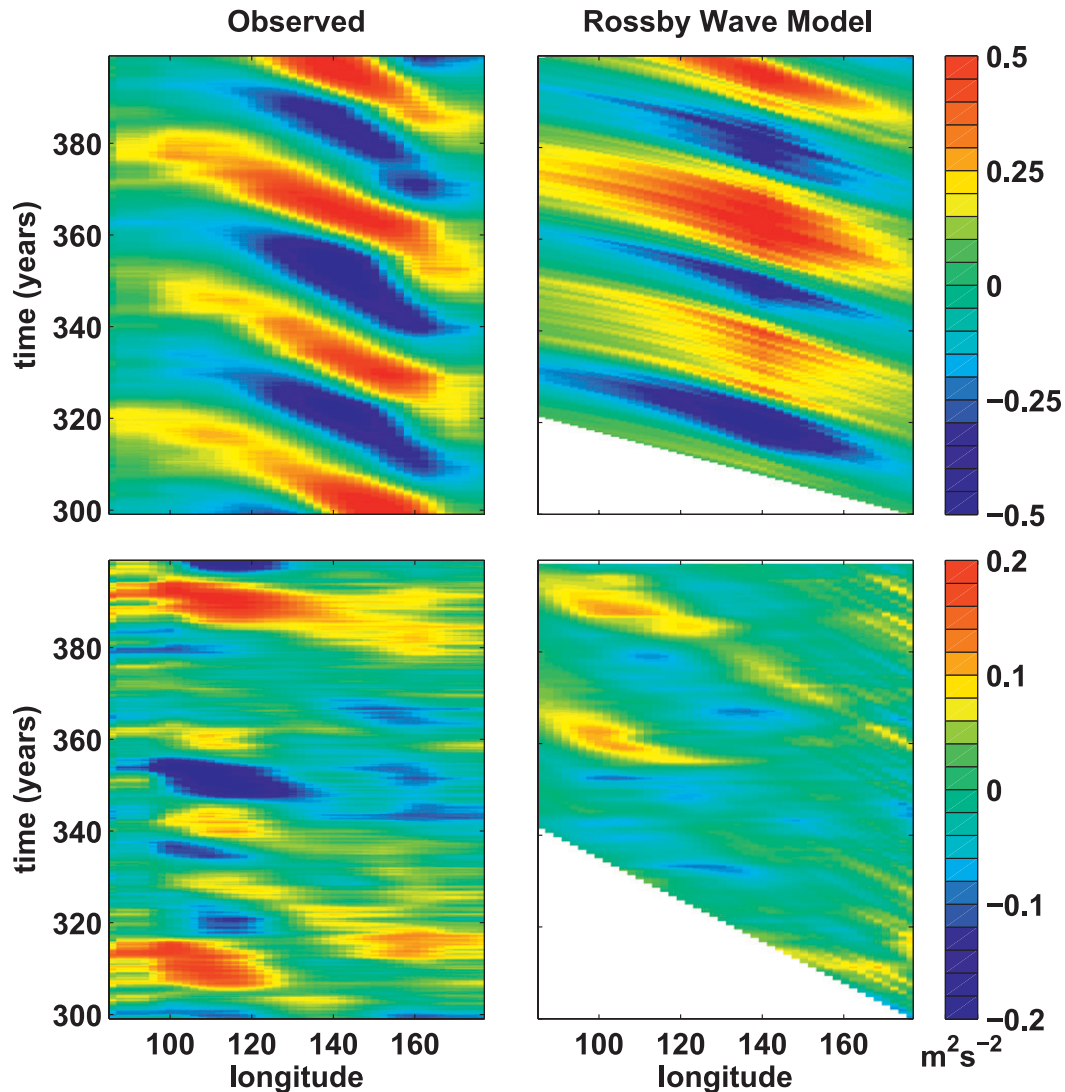


FIG. 13. Hovmöller plot of baroclinic pressure anomalies ( $\text{m}^2 \text{s}^{-2}$ ) averaged within the latitude range  $55^\circ\text{--}60^\circ\text{N}$  from (left) the model ( $p'_{bc}$ ) and (right) predicted from the Rossby wave model ( $p'_r$ ) for (top) Flat and (bottom) Bowl.

projected onto the first baroclinic mode) in the model averaged over the latitude range  $55^\circ\text{--}65^\circ\text{N}$  as a function of longitude and time. Note the similarity between the  $p'_{bc}$  and the buoyancy anomalies at a depth of 265 m (see Fig. 9). Positive (negative) buoyancy anomalies are associated with a thicker (thinner) thermocline and high (low) sea surface heights, and thus a positive (negative) value of  $p'_{bc}$ . The right panels of Fig. 13 show  $p'_r$ , the baroclinic pressure potential anomalies calculated from the Rossby wave model. The Rossby wave model successfully captures the basic character of  $p'_{bc}$  in both Flat and Bowl. In Flat westward-propagating pressure (and buoyancy) anomalies are found over the entire width of the basin. In Bowl the largest baroclinic pressure anomalies are restricted to the western part of the basin.

Furthermore, the Rossby wave model can be used to determine if  $p_{bc}$  anomalies originate on the eastern boundary or are the result of windstress forcing integrated along Rossby wave characteristics. In Flat  $p'_r$  is dominated by the eastern boundary contribution. In contrast, in Bowl the eastern boundary contribution is negligible and  $p'_r$  is dominated by windstress forcing integrated along Rossby wave characteristics (not shown). Application of Rossby wave models to observations generally shows that in mid to high latitudes the influence of the eastern boundary only propagates a few hundred kilometers from the boundary, and most of the variability in the interior is due to stochastic wind forcing integrated along Rossby wave characteristics (Qiu and Müller 1997; Fu and Qui 2002; Qiu and Chen 2006).

We can also use the Rossby wave model to understand the shape of the spectra of the WBB index (and hence the MOC index). Frankignoul et al. (1997) demonstrate that if the forcing is white, in the absence of dissipation the power spectrum of the baroclinic response is red with a  $-2$  slope at high frequencies and flattens out to a constant level at frequencies longer than the time it takes for a baroclinic Rossby wave to propagate across the basin. Sirven et al. (2002) consider how the spectrum of the baroclinic response is modified by dissipation.<sup>9</sup> They find that dissipation does not alter the low frequency response, but it leads to a spectral decay at high frequencies that is faster than  $\omega^{-2}$ . In both Flat and Bowl, the spectrum of the WBB index is red with a slope slightly steeper than  $\omega^{-2}$  ( $-2.21$  for Flat and  $-2.24$  for Bowl) at high frequencies and flattens out to a constant value at low frequencies. The transition from a red spectrum to a flat spectrum occurs at approximately the time it takes for a baroclinic Rossby wave to propagate across the basin. The presence of the peak in the power spectrum in Flat is due to very regular Rossby waves that originate from the eastern boundary.

#### f. Relationship between upper-ocean and deep anomalies

A central question regarding variability of the AMOC is the mechanism by which buoyancy anomalies make their way from the upper ocean, where numerous processes can lead to buoyancy variability, to the deep ocean where they can influence the strength of the MOC. Oftentimes, convection is implicated for communicating anomalies from the surface to depth or for leading to vertical velocity anomalies (despite the connection between convection and vertical velocities being very tenuous). Our explanation for how upper-ocean buoyancy anomalies lead to changes in the MOC is much simpler (and we believe more compelling). Upper-ocean buoyancy anomalies travel westward as baroclinic Rossby waves. Although their signal is larger near the surface, they have an expression at depth. (Note the different color scales for the buoyancy section at  $60^\circ\text{N}$  and the buoyancy anomalies along the boundaries in Figs. 6 and 7: the anomalies in the upper ocean are about 5 times larger.) The vertical structure of the first baroclinic mode (zonally averaged over the latitude range  $55^\circ$ – $65^\circ\text{N}$ ) is plotted in the top-left panel of Fig. 14. Note that the baroclinic depth scale  $h/\phi_1(0)$  (Frankignoul et al. 1997, see appendix) is  $O(1.5 \text{ km})$  in the subpolar gyre. Thus, no complex mechanism is needed for buoyancy

anomalies to reach the deep ocean. The buoyancy anomalies merely travel southward along the western boundary following the mean isopycnals.

#### g. Discussion

The essential result of this section is that the MOC does not play an active role in creating the decadal buoyancy anomalies in the model. The observed (lagged) correlation between decadal buoyancy and MOC anomalies is due to the thermal wind relation. Buoyancy anomalies originate in the upper ocean of the subpolar gyre. Upon reaching the western boundary, they are advected southward by the deep western boundary current, leading to latitudinally coherent AMOC variability. While the origin of the buoyancy anomalies in the subpolar gyre differs between Flat and Bowl, in both cases they are linked to baroclinic Rossby waves.

Rossby waves originating on the eastern boundary, which grow by extracting energy from the mean flow as they travel westward, are the dominant source of buoyancy variability in Flat. These waves do not require stochastic atmospheric variability to exist. A standard linear stability analysis (not shown) indicates that the eastern boundary current is unstable. In Flat the instability of the eastern boundary current is able to radiate into the interior (Walker and Pedlosky 2002; Hristova et al. 2008; Wang 2011) and excites the least damped basin mode, which has wavelength one across the basin (Cessi and Primeau 2001; Spydell and Cessi 2003). The dominance of this mode explains the large peak in the spectra of the MOC and WBB at a time scale of 34 yr. It is a well known result that basin modes are attenuated when bathymetry is added to models (Ripa 1978), which can explain the lack of regular waves emanating from the eastern boundary in Bowl.

The buoyancy variability in Bowl is explained to a large degree by stochastic wind forcing integrated along Rossby wave characteristics. However, ocean-only experiments suggest that both buoyancy and wind forcing are capable of exciting buoyancy and MOC variability in Bowl. Therefore, we could likely improve the baroclinic Rossby wave model discussed in section 4e by including buoyancy as well as wind forcing. Buoyancy forcing is likely to play a larger role in the subpolar gyre than in the subtropics since deep mixed layers may allow buoyancy forcing to penetrate deep enough to force the first baroclinic mode. Furthermore, as discussed in section 4d, internal ocean instabilities likely play a role in creating buoyancy anomalies near the western boundary. Thus, buoyancy anomalies in Bowl are due to a mixture of processes, including wind (and perhaps buoyancy) forced Rossby waves and baroclinic instability of western boundary currents.

<sup>9</sup> They consider Laplacian dissipation rather than linear dissipation.



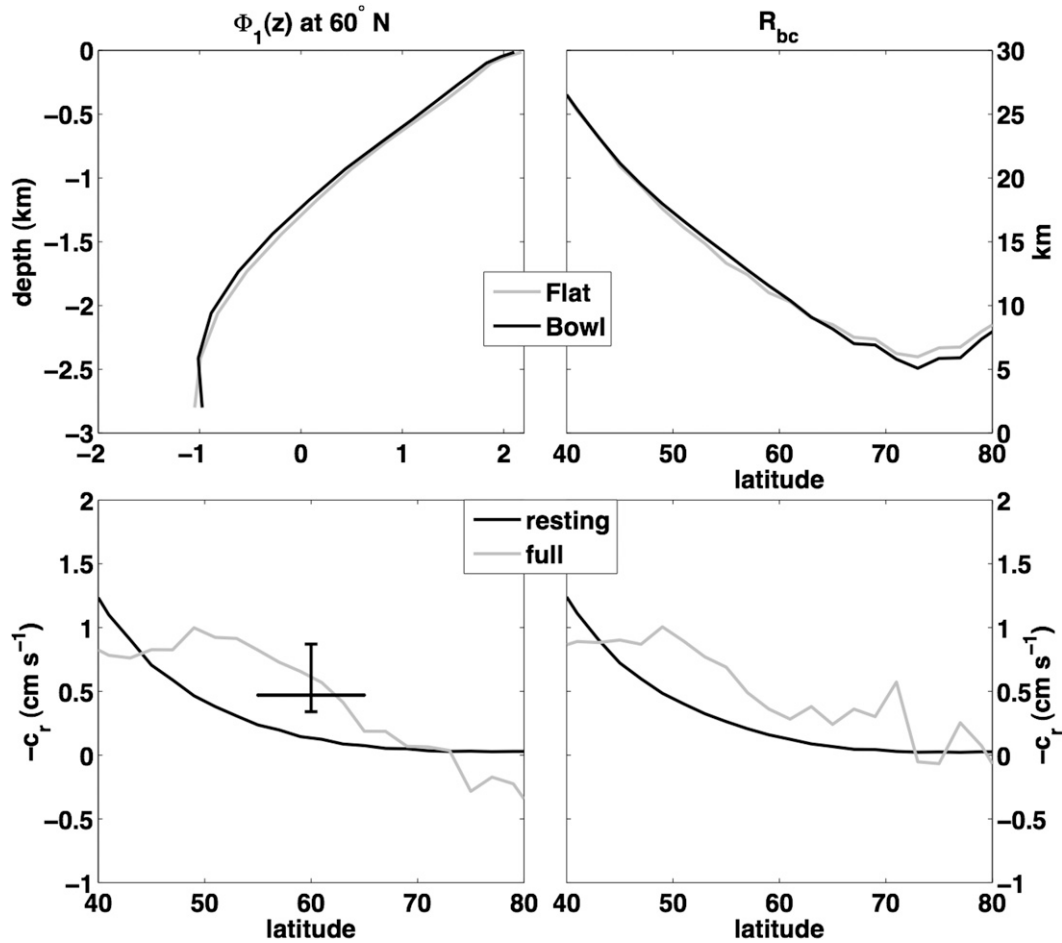


FIG. 14. (top) (left) Vertical structure  $\phi_1$  and (right) deformation radius  $R_1$  of the first baroclinic mode, zonally averaged over the small basin for Flat (grey lines) and Bowl (black lines). (bottom) Predicted westward phase speeds of first baroclinic long Rossby waves zonally averaged over the small basin for (left) Flat and (right) Bowl. Two different estimates of the phase speed are included: the predicted phase speed for a resting ocean (black lines) and the predicted phase speed when the mean flow and PV gradients are included (gray lines). The black error bars in the bottom-left panel show the observed phase speed of the waves in Flat. These phase speeds were calculated for buoyancy anomalies averaged over the latitude range 55°–60°N.

While we think it is likely that the real ocean looks more like Bowl, we would like to stress that we are not suggesting that the buoyancy variability in either Flat or Bowl is particularly realistic. However, we believe that the processes that lead to the decadal buoyancy anomalies in our models, including wind (and perhaps buoyancy) forced Rossby waves and baroclinic instability of western boundary currents, likely play a role in decadal buoyancy variability in the real ocean. Additionally, both more realistic models (Danabasoglu 2008; Zhang 2008; Tulloch and Marshall 2012) and data (Kwon et al. 2010) show that decadal buoyancy anomalies are largest along the western boundary of the subtropical gyre and along the boundary between the subtropical and subtropical gyres, which is exactly the

region where the largest buoyancy anomalies are found in our models.

## 5. Conclusions

Coupled and ocean-only GCMs run in idealized geometries are used to study the relationships between decadal MOC and buoyancy variability. Our main results are as follows:

- (i) Decadal MOC variability in the subtropical oceans is related to buoyancy anomalies on the western boundary according to the thermal wind relation. Ageostrophic (Ekman) MOC anomalies are negligible on decadal time scales.

- (ii) The upper ocean of the subpolar gyre is identified as a key region for monitoring the MOC. Buoyancy anomalies originate in the upper ocean of the subpolar gyre, travel to the western boundary as baroclinic Rossby waves, and are advected southward by the DWBC, leading to latitudinally coherent MOC variability.
- (iii) The MOC does not play an active role in setting upper-ocean buoyancy (or SST) on decadal time scales. Although changes in the MOC do lead to changes in OHT, these OHT anomalies are not responsible for creating decadal buoyancy anomalies in the subpolar gyre.

An obvious question is whether our results are robust. Can decadal AMOC variability in nature be explained simply as the thermal wind response to buoyancy anomalies which originate in the subpolar gyre and travel southward along the western boundary? In nature, is the AMOC also passive on decadal time scales or does it play an active role in creating decadal buoyancy anomalies?

One piece of evidence that our results are robust is a comparison between our two model setups. Despite the different origin and spatial/temporal patterns of buoyancy variability in Flat and Bowl, the relationship between MOC and buoyancy variability is virtually identical. In both cases, MOC variability is associated with upper-ocean buoyancy anomalies in the subpolar gyre. When these buoyancy anomalies reach the western boundary, they travel southward in the DWBC, leading to latitudinally coherent MOC variability. Most importantly, in both models the MOC is passive.

Comparisons of our results to other models, both idealized models and more complex GCMs, also suggest that our results are robust. Several idealized (Zanna et al. 2011b) and complex (Danabasoglu 2008; Zhang 2008; Tziperman et al. 2008; Hawkins and Sutton 2009) GCMs have linked MOC variability to upper-ocean buoyancy anomalies in the subpolar gyre. Idealized model studies (te Raa and Dijkstra 2002) and GCM studies (te Raa et al. 2004; Hirschi et al. 2007; Frankcombe and Dijkstra 2009; Zanna et al. 2011a,b) have previously linked MOC variability to baroclinic Rossby waves and suggested that the dominant time scale of MOC variability is related to the time it takes for baroclinic Rossby waves to propagate across the basin. Furthermore, in a study inspired by this work, Tulloch and Marshall (2012) find that in CCSM3 and the Geophysical Fluid Dynamics Laboratory Coupled Model (CM2.1), buoyancy anomalies on the western boundary near the Grand Banks are related to AMOC variability in accord with the thermal

wind relation, in direct parallel with our idealized model studies.

Despite the prevalence of the “active” MOC hypothesis in the literature, several other modeling studies have suggested that the AMOC does not play a significant role in the creation of decadal buoyancy anomalies. Danabasoglu (2008) shows that decadal buoyancy anomalies in CCSM3 are due to fluctuations in the boundary between the subtropical and subpolar gyres due to wind stress curl variability associated with the North Atlantic Oscillation (NAO). He hypothesizes that the observed (lagged) correlation between these buoyancy anomalies and the AMOC is due to changes in deep-water formation that result when these anomalies enter the Labrador Sea. In an idealized model study Zanna et al. (2011b) found that large amplification of upper-ocean temperature anomalies can occur due to nonnormal dynamics without active participation of the AMOC.

Determining whether our results are applicable to the real ocean is, of course, more difficult, but a number of ocean observations support our results. In nature, significant decadal buoyancy anomalies are found near the western boundary of the subpolar gyre and along the boundary between the subtropical and subpolar gyres (Kwon et al. 2010). This location is exactly where we find buoyancy anomalies to be important in changing the strength of the MOC in our idealized models. Thus, we expect that in nature decadal AMOC variability is likely related to buoyancy anomalies that originate in the subpolar gyre and travel southward along the western boundary. Furthermore, tracking of temperature and potential vorticity anomalies in the DWBC (Curry et al. 1998; Peña-Molino et al. 2011) suggests that these anomalies travel at advective speeds, just like in our idealized models.

Determining whether the AMOC plays an active role in setting SST on decadal time scales in nature is extremely difficult. However, a number of studies suggest that low-frequency upper-ocean buoyancy and sea surface height variability in the Atlantic may be fully explained by processes such as wind/buoyancy forced Rossby waves (Sturges et al. 1998) and internal ocean instability. If these well understood processes can explain most of the observed decadal SST variability, there may be no need to invoke the AMOC as an active player in the climate system on decadal time scales.

Finally, our model study highlights the need for studies that examine the role (or lack thereof) that meridional OHT anomalies associated with the AMOC play in creating decadal buoyancy anomalies. The simplicity and robustness of our result suggests that a “passive AMOC view” could be used as a null hypothesis when exploring SST and AMOC variability in observations and more complex GCMs.

Our results, if robust, carry significant implications for decadal observations and predictions.

- (i) If the AMOC is truly passive, knowledge of AMOC variability in the subtropical gyre will not enable the prediction of decadal SST anomalies. Instead, predictability may be related to the evolution of upper-ocean temperature anomalies, perhaps due to wind/buoyancy forced Rossby waves (Sturges et al. 1998; Schneider and Miller 2001), internal instability, or nonnormal growth (Tziperman et al. 2008; Hawkins and Sutton 2009; Zanna et al. 2011a,b).
- (ii) Since decadal buoyancy anomalies originate in the subpolar gyre, observing systems for making decadal predictions should monitor upper-ocean buoyancy anomalies in the subpolar gyre. The importance of monitoring the subpolar gyre was previously pointed out by Tziperman et al. (2008), Hawkins and Sutton (2009), and Zanna et al. (2011b), who found that nonnormal growth of upper-ocean buoyancy anomalies in the far North Atlantic led to basinwide AMOC and buoyancy variability. Bingham et al. (2007) also pointed out the importance of monitoring the subpolar gyre, albeit for a different reason: in their models AMOC anomalies on interannual time scales were not coherent between the subtropical and subpolar gyres. Our results further confirm the importance of the subpolar gyre by unequivocally demonstrating that growth of buoyancy anomalies in the subpolar gyre can occur without active participation of the large-scale AMOC.

*Acknowledgments.* We thank Jim Todd at NOAA for providing funding for this research at MIT through the U.S. Climate Variability and Predictability (CLIVAR) Program. Funding for the portion of the work done at AER was provided by NOAA Grant NA10OAR4310199 (Climate Variability and Predictability). We would also like to thank three anonymous reviewers for their comments, which certainly helped sharpen the content of the manuscript.

## APPENDIX

### Spinup of Ocean Circulation by Rossby Waves

Here, we estimate the decadal response of the extratropical ocean to forcing, following White (1977) and Frankignoul et al. (1997). At each latitude the baroclinic response of the ocean to forcing is governed by the long Rossby wave equation:

$$\frac{\partial p_r}{\partial t} + c_r \frac{\partial p_r}{\partial x} = F(x, t) + \epsilon p_r. \quad (\text{A1})$$

In a continuously stratified ( $N$  level) model, we identify the baroclinic response with the first mode  $\phi_1$  of an infinite set (set of  $N$ ) of baroclinic modes, and hence  $c_r$  is the (zonal) phase speed of the first baroclinic Rossby wave. Here  $p_r(x, y, t)$  is given by the pressure potential  $p(x, y, t)$  (dynamic pressure divided by reference density  $\rho_0$ ) projected onto the vertical structure of the first baroclinic mode  $\phi_1(z)$ :

$$p(x, y, z, t) = p_r(x, y, t)\phi_1(z).$$

The forcing  $F(x, t)$  (also projected onto the first baroclinic mode) may be wind forcing and/or buoyancy forcing. Higher-order baroclinic modes are assumed not to be important and are not considered here. In Eq. (A1)  $\epsilon < 0$  represents the role of dissipation (Qiu and Müller 1997), but we also allow  $\epsilon > 0$  in order to represent internal sources of anomalies of  $p_r$  due to, for example, baroclinic instability.

At each latitude Eq. (A1) can be solved using the method of characteristics, integrating from the eastern boundary ( $x = x_e$ ):

$$p_r(x, t) = \frac{1}{u(x)} p_r \left( x_e, t - \frac{x - x_e}{c_r} \right) + \frac{1}{u(x)} \int_{x_e}^x \frac{1}{c_r} F \left( x', t - \frac{x - x'}{c_r} \right) u(x') dx', \quad (\text{A2})$$

where

$$u(x) = \exp \int_{x_e}^x -\frac{\epsilon}{c_r} dx'.$$

The first term represents the westward propagation of anomalies originating on the eastern boundary into the interior, and the second term is the variability due to the forcing  $F(x, t)$  integrated along Rossby wave characteristics. If  $\epsilon$  and  $c_r$  are constant, this reduces to

$$p_r(x, t) = p_r \left( x_e, t - \frac{x - x_e}{c_r} \right) \exp \frac{\epsilon}{c_r} (x - x_e) + \int_{x_e}^x \frac{1}{c_r} F \left( x', t - \frac{x - x'}{c_r} \right) \exp \frac{\epsilon}{c_r} (x - x') dx'. \quad (\text{A3})$$

Generally,  $F(x, t)$  is taken to be the response of the ocean to windstress forcing (Flierl 1978; Frankignoul et al. 1997; Codiga and Cornillon 2003):

$$F(x, t) = -\frac{f^2}{h}\phi_1(0)R_{bc}^2w_e, \quad (\text{A4})$$

where  $f$  is the Coriolis parameter,  $h$  is the ocean depth, and  $R_{bc}$  is the deformation radius. The Ekman velocity  $w_e$  is given by

$$w_e = \frac{1}{\rho_o} \text{curl}_z \left( \frac{\tau}{f} \right),$$

where  $\tau$  is the wind stress.

### Application of Rossby wave model

The vertical structure  $\phi_1(z)$ , deformation radius  $R_{bc}$ , and phase velocity  $c_r$  of the first baroclinic mode are required inputs to our Rossby wave model. We briefly describe how these parameters are calculated from the model. Seeking wave solutions to the quasigeostrophic potential vorticity equation results in the standard Sturm–Liouville problem (Gill 1982), whose eigenvectors  $\phi_n$  give the vertical structure and whose eigenvalues ( $K_n$ ) give the deformation wavenumbers. We chose to make the assumption of a resting ocean in the calculation of the vertical structure because in this case the eigenfunctions  $\phi_n$  form an orthonormal basis. In practice there is little difference between the vertical structure predictions for a resting ocean and one with mean currents (Wunsch 1997). The vertical structure of the first baroclinic mode  $\phi_1(z)$  and the deformation radius  $R_{bc} \equiv K_1^{-1}$  (zonally averaged over the small basin) are shown in the top panels of Fig. 14. Two different estimates of the phase speed (also zonally averaged over the small basin) are shown in Fig. 14 (bottom panels): the predicted phase speed for a resting ocean (black lines) and the predicted phase speed when the mean flow and potential vorticity gradients are included (gray lines), as described in Tulloch et al. (2009). Also included in Fig. 14 is the range of phase speeds seen in Flat at 60°N (black error bars). The phase speed of the buoyancy anomalies is consistent with the phase speed of long first baroclinic Rossby waves when the mean flow and the full mean potential vorticity gradient are included in the calculation.

Now we can compare  $p'_{bc}$ , the baroclinic pressure potential anomalies in the coupled model, to  $p'_r$ , the baroclinic pressure potential anomalies calculated from the Rossby wave model [Eq. (A2)]. Baroclinic pressure anomalies  $p'_{bc}(x, y, t)$  are computed from the model's pressure potential by projecting pressure potential anomalies onto  $\phi_1$ . The left panels of Fig. 13 show  $p'_{bc}$  averaged over the latitude range 55°–65°N as a function of longitude and time. Calculating  $p'_r$  involves the evaluation of two terms. The first term in Eq. (A2) is calculated from  $p'_{bc}$  on the eastern boundary, averaged

over the latitude range 55°–65°N. Ekman pumping anomalies calculated from the model's windstress field are averaged over the latitude range 55°–65°N and integrated along Rossby wave characteristics to calculate the second term in Eq. (A2). Here  $\epsilon$  is assumed to be a negative constant (no variation with longitude) except in the eastern part of the basin in Flat where we allow  $\epsilon$  to be positive to represent internal sources of  $p'_r$  (see section 4d). A range of (piecewise constant) values of  $\epsilon$  are tested, and we chose the  $\epsilon$  that leads to the modeled  $p'_r$  matching the observed  $p'_{bc}$  most closely. We find that for Flat  $\epsilon = 1/6 \text{ yr}^{-1}$  in the eastern part of the basin ( $x \geq 160^\circ$ ) and  $\epsilon = -1/10 \text{ yr}^{-1}$  in the western part of the basin ( $x < 160^\circ$ ) and for Bowl  $\epsilon = -1/8 \text{ yr}^{-1}$ . The right panels of Fig. 13 show  $p'_r$ , the baroclinic pressure anomalies calculated from the Rossby wave model.

### REFERENCES

- Adcroft, A., and J.-M. Campin, 2004: Rescaled height coordinates for accurate representation of free-surface flows in ocean circulation models. *Ocean Modell.*, **7** (3–4), 269–284, doi:10.1016/j.ocemod.2003.09.003.
- , —, C. Hill, and J. Marshall, 2004: Implementation of an atmosphere–ocean general circulation model on the expanded spherical cube. *Mon. Wea. Rev.*, **132**, 2845–2863.
- Baehr, J., J. Hirschi, J.-O. Beismann, and J. Marotzke, 2004: Monitoring the meridional overturning circulation in the North Atlantic: A model-based array design study. *J. Mar. Res.*, **62**, 283–312.
- Bingham, R., C. Hughes, V. Roussenov, and R. Williams, 2007: Meridional coherence of the North Atlantic meridional overturning circulation. *Geophys. Res. Lett.*, **34**, L23606, doi:10.1029/2007GL031731.
- Bjerknes, J., 1964: Atlantic air–sea interaction. *Advances in Geophysics*, Vol. 10, Academic Press, 1–82.
- Boccaletti, G., R. Ferrari, A. Adcroft, D. Ferreira, and J. Marshall, 2005: The vertical structure of ocean heat transport. *Geophys. Res. Lett.*, **32**, L10603, doi:10.1029/2005GL022474.
- Cabanes, C., T. Lee, and L. Fu, 2008: Mechanisms of interannual variations of the meridional overturning circulation of the North Atlantic Ocean. *J. Phys. Oceanogr.*, **38**, 467–480.
- Campin, J.-M., J. Marshall, and D. Ferreira, 2008: Sea ice–ocean coupling using a rescaled vertical coordinate  $z^*$ . *Ocean Modell.*, **24**, 1–14, doi:10.1016/j.ocemod.2008.05.005.
- Cayan, D., 1992a: Latent and sensible heat flux anomalies over the northern oceans: Driving the sea surface temperature. *J. Phys. Oceanogr.*, **22**, 859–881.
- , 1992b: Latent and sensible heat flux anomalies over the northern oceans: The connection to monthly atmospheric circulation. *J. Climate*, **5**, 354–369.
- Cessi, P., and F. Primeau, 2001: Dissipative selection of low-frequency modes in a reduced-gravity basin. *J. Phys. Oceanogr.*, **31**, 127–137.
- Codiga, D., and P. Cornillon, 2003: Effects of geographical variation in vertical mode structure on the sea surface topography, energy, and wind forcing of baroclinic Rossby waves. *J. Phys. Oceanogr.*, **33**, 1219–1230.
- Colin de Verdière, A., and T. Huck, 1999: Baroclinic instability: An oceanic wavemaker for interdecadal variability. *J. Phys. Oceanogr.*, **29**, 893–910.

- Cunningham, S., and Coauthors, 2007: Temporal variability of the Atlantic meridional overturning circulation at 26.5°N. *Science*, **317**, 935–937.
- Curry, R. G., M. S. McCartney, and T. M. Joyce, 1998: Oceanic transport of subpolar climate signals to mid-depth subtropical waters. *Nature*, **391**, 575–577.
- Danabasoglu, G., 2008: On multidecadal variability of the Atlantic meridional overturning circulation in the Community Climate System Model, version 3. *J. Climate*, **21**, 5524–5544.
- Delworth, T., and M. Mann, 2000: Observed and simulated multidecadal variability in the Northern Hemisphere. *Climate Dyn.*, **16**, 661–676.
- , S. Manabe, and R. Stouffer, 1993: Interdecadal variations in the thermohaline circulation in a coupled ocean–atmosphere model. *J. Climate*, **6**, 1993–2011.
- Deser, C., and M. L. Blackmon, 1993: Surface climate variations over the North Atlantic Ocean during winter: 1900–1989. *J. Climate*, **6**, 1743–1753.
- Deshayes, J., and C. Frankignoul, 2005: Spectral characteristics of the response of the meridional overturning circulation to deep-water formation. *J. Phys. Oceanogr.*, **35**, 1813–1825.
- Dong, B., and R. Sutton, 2001: The dominant mechanisms of variability in Atlantic Ocean heat transport in a coupled ocean–atmospheric GCM. *Geophys. Res. Lett.*, **28**, 2445–2448.
- , and —, 2003: Variability of Atlantic Ocean heat transport and its effects on the atmosphere. *Ann. Geophys.*, **46**, 87–97.
- Dong, S., and K. A. Kelly, 2004: Heat budget in the Gulf Stream region: The importance of heat storage and advection. *J. Phys. Oceanogr.*, **34**, 1214–1231.
- , S. L. Hautala, and K. A. Kelly, 2007: Interannual variations in upper-ocean heat content and heat transport convergence in the western North Atlantic. *J. Phys. Oceanogr.*, **37**, 2682–2697.
- Ferrari, R., and D. Ferreira, 2011: What processes drive the ocean heat transport? *Ocean Modell.*, **38** (3–4), 171–186, doi:10.1016/j.ocemod.2011.02.013.
- Ferreira, D., J. Marshall, and J.-M. Campin, 2010: Localization of deep-water formation: Role of atmospheric moisture transport and geometrical constraints on ocean circulation. *J. Climate*, **23**, 1456–1476.
- Flierl, G. R., 1978: Models of vertical structure and the calibration of two-layer models. *Dyn. Atmos. Oceans*, **2**, 341–381, doi:10.1016/0377-0265(78)90002-7.
- Frankcombe, L. M., and H. A. Dijkstra, 2009: Coherent multidecadal variability in North Atlantic sea level. *Geophys. Res. Lett.*, **36**, L15604, doi:10.1029/2009GL039455.
- Frankignoul, C., P. Müller, and E. Zorita, 1997: A simple model of the decadal response of the ocean to stochastic wind forcing. *J. Phys. Oceanogr.*, **27**, 1533–1546.
- , A. Czaja, and B. L'Heveder, 1998: Air–sea feedback in the North Atlantic and surface boundary conditions for ocean models. *J. Climate*, **11**, 2310–2324.
- Fu, L., and B. Qui, 2002: Low-frequency variability of the North Pacific Ocean the roles of boundary- and wind-driven baroclinic rossby waves. *J. Geophys. Res.*, **107** (C12), 3220, doi:10.1029/2001JC001131.
- Ganachaud, A., and C. Wunsch, 2003: Large-scale ocean heat and freshwater transports during the World Ocean Circulation Experiment. *J. Climate*, **16**, 696–705.
- Gent, P. R., and J. C. McWilliams, 1990: Isopycnal mixing in ocean circulation models. *J. Phys. Oceanogr.*, **20**, 150–155.
- Gill, A., 1982: *Atmosphere–Ocean Dynamics*. Academic Press, 662 pp.
- Grist, J., and Coauthors, 2010: The roles of surface heat flux and ocean heat transport convergence in determining Atlantic Ocean temperature variability. *Ocean Dyn.*, **60**, 771–790, doi:10.1007/s10236-010-0292-4.
- Hasselmann, K., 1976: Stochastic climate models. Part I: Theory. *Tellus*, **28**, 289–305.
- Hawkins, E., and R. Sutton, 2009: Decadal predictability of the Atlantic Ocean in a coupled GCM: Forecast skill and optimal perturbations using linear inverse modeling. *J. Climate*, **22**, 3960–3978.
- Hirschi, J., and J. Marotzke, 2007: Reconstructing the meridional overturning circulation from boundary densities and the zonal wind stress. *J. Phys. Oceanogr.*, **37**, 743–763, doi:10.1175/JPO3019.1.
- , P. Killworth, and J. Blundel, 2007: Subannual, seasonal, and interannual variability of the North Atlantic meridional overturning circulation. *J. Phys. Oceanogr.*, **37**, 1246–1265.
- Hristova, H. G., J. Pedlosky, and M. A. Spall, 2008: Radiating instability of a meridional boundary current. *J. Phys. Oceanogr.*, **38**, 2294–2307.
- Johns, W. E., and Coauthors, 2010: Continuous, array-based estimates of Atlantic Ocean heat transport at 26.5°N. *J. Climate*, **24**, 2429–2449.
- Johnson, H. L., and D. P. Marshall, 2002a: A theory for the surface Atlantic response to thermohaline variability. *J. Phys. Oceanogr.*, **32**, 1121–1132.
- , and —, 2002b: Localization of abrupt change in the North Atlantic thermohaline circulation. *Geophys. Res. Lett.*, **29**, 1083, doi:10.1029/2001GL014140.
- Kanzow, T., U. Send, W. Zenk, A. Chave, and M. Rhein, 2006: Monitoring the integrated deep meridional flow in the tropical North Atlantic: Long-term performance of a geostrophic array. *Deep-Sea Res. I*, **53**, 528–546.
- Kawase, M., 1987: Establishment of deep ocean circulation driven by deep-water production. *J. Phys. Oceanogr.*, **17**, 2294–2317.
- Klinger, B., J. Marshall, and U. Send, 1996: Representation of convective plumes by vertical adjustment. *J. Geophys. Res.*, **101** (C8), 18 175–18 182.
- Knight, J., R. Allan, C. Follard, and M. Vellinga, 2005: A signature of persistent natural thermohaline circulation cycles in observed climate. *Geophys. Res. Lett.*, **32**, L20708, doi:10.1029/2005GL024233.
- Kushnir, Y., 1994: Interdecadal variations in North Atlantic sea surface temperatures and associated atmospheric conditions. *J. Climate*, **9**, 1208–1220.
- Kwon, Y.-O., M. Alexander, N. Bond, C. Frankignoul, H. Nakamura, B. Qiu, and L. A. Thompson, 2010: Role of the Gulf Stream and Kuroshio–Oyashio systems in large-scale atmosphere–ocean interaction: A review. *J. Climate*, **23**, 3249–3281.
- Lee, T., and J. Marotzke, 1998: Seasonal cycles of meridional overturning and heat transport of the Indian Ocean. *J. Phys. Oceanogr.*, **28**, 923–943.
- Lozier, M. S., 2010: Deconstructing the conveyor belt. *Science*, **328**, 1507–1511, doi:10.1126/science.1189250.
- Mann, M., J. Park, and R. Bradley, 1995: Global interdecadal and century-scale oscillations during the past five centuries. *Nature*, **378**, 266–270.
- , R. Bradley, and M. Hughes, 1998: Global-scale temperature patterns and climate forcing over the past six centuries. *Nature*, **392**, 779–787.
- Marotzke, J., and B. A. Klinger, 2000: The dynamics of equatorially asymmetric thermohaline circulations. *J. Phys. Oceanogr.*, **30**, 955–970.
- Marshall, J., A. Adcroft, C. Hill, L. Perelman, and C. Heisey, 1997: A finite-volume, incompressible Navier Stokes model for

- studies of the ocean on parallel computers. *J. Geophys. Res.*, **102** (C2), 5753–5766.
- Molteni, F., 2003: Atmospheric simulations using a GCM with simplified physical parameterizations. I: Model climatology and variability in multidecadal experiments. *Climate Dyn.*, **20**, 175–191.
- Msadek, R., and C. Frankignoul, 2009: Atlantic multidecadal oceanic variability and its influence on the atmosphere in a climate model. *Climate Dyn.*, **33**, 45–62.
- Peña-Molino, B., T. Joyce, and J. Toole, 2011: Recent changes in the Labrador Sea Water within the deep western boundary current southeast of Cape Cod. *Deep-Sea Res. I*, **58**, 1019–1030.
- Qiu, B., 2002: Large-scale variability in the midlatitude subtropical and subpolar ocean: Observations and causes. *J. Phys. Oceanogr.*, **32**, 353–375.
- , and P. Müller, 1997: Propagation and decay of forced and free baroclinic Rossby waves in off-equatorial oceans. *J. Phys. Oceanogr.*, **27**, 2405–2417.
- , and S. Chen, 2006: Decadal variability in the large-scale sea surface height field of the South Pacific Ocean: Observations and causes. *J. Phys. Oceanogr.*, **36**, 1751–1762.
- Redi, M. H., 1982: Oceanic isopycnal mixing by coordinate rotation. *J. Phys. Oceanogr.*, **12**, 1154–1158.
- Ripa, P., 1978: Normal Rossby basin modes of a closed basin with topography. *J. Geophys. Res.*, **83** (C4), 1947–1957.
- Schneider, N., and A. Miller, 2001: Predicting western North Pacific Ocean climate. *J. Climate*, **14**, 3997–4002.
- Seager, R., Y. Kushnir, P. Chang, N. Naik, J. Miller, and W. Hazeleger, 2000: Causes of Atlantic Ocean climate variability between 1958 and 1998. *J. Climate*, **13**, 2845–2862.
- Shaffrey, L., and R. Sutton, 2006: Bjerknes compensation and the decadal variability of the energy transports in a coupled climate model. *J. Climate*, **19**, 1167–1181, doi:10.1175/JCLI3652.1.
- Sime, L., D. Stevens, K. Heywood, and K. Oliver, 2006: A decomposition of the Atlantic meridional overturning. *J. Phys. Oceanogr.*, **36**, 2253–2270.
- Sirven, J., C. Frankignoul, D. DeCoetlogon, and V. Tailandier, 2002: Spectrum of wind-driven baroclinic fluctuations of the ocean in the midlatitudes. *J. Phys. Oceanogr.*, **32**, 2405–2417.
- Spence, P., O. Saenko, W. Sijp, and M. England, 2012: The role of bottom pressure torques in the interior pathways of North Atlantic Deep Water. *J. Phys. Oceanogr.*, **42**, 110–125.
- Spydell, M., and P. Cessi, 2003: Baroclinic modes in a two-layer basin. *J. Phys. Oceanogr.*, **33**, 610–622.
- Sturges, W., and B. Hong, 1995: Wind forcing of the Atlantic thermocline along 32°N at low frequency. *J. Phys. Oceanogr.*, **25**, 1706–1715.
- , —, and A. Clark, 1998: Decadal wind forcing of the North Atlantic subtropical gyre. *J. Phys. Oceanogr.*, **28**, 659–698.
- Talley, L., 2003: Shallow, intermediate, and deep overturning components of the global heat budget. *J. Phys. Oceanogr.*, **33**, 530–560.
- te Raa, L. A., and H. A. Dijkstra, 2002: Instability of the thermohaline ocean circulation on interdecadal timescales. *J. Phys. Oceanogr.*, **32**, 138–160.
- , J. Gerrits, and H. A. Dijkstra, 2004: Identification of the mechanism of interdecadal variability in the North Atlantic Ocean. *J. Phys. Oceanogr.*, **34**, 2792–2807.
- Ting, M., Y. Kushnir, R. Seager, and C. Li, 2009: Forced and internal twentieth-century SST trends in the North Atlantic. *J. Climate*, **22**, 1469–1481.
- Toole, J., R. Curry, T. Joyce, M. McCartney, and B. Peña-Molino, 2011: Transport of the North Atlantic deep western boundary current about 39°N, 70°W: 2004–2008. *Deep-Sea Res. II*, **58**, 1768–1780.
- Trenberth, K. E., and J. M. Caron, 2001: Estimates of meridional atmosphere and ocean heat transports. *J. Climate*, **14**, 3433–3443.
- Tulloch, R., and J. Marshall, 2012: Exploring mechanisms of variability and predictability of Atlantic meridional overturning circulation in two coupled climate models. *J. Climate*, **25**, 4067–4080.
- , —, and K. S. Smith, 2009: Interpretation of the propagation of surface altimetric observations in terms of planetary waves and geostrophic turbulence. *J. Geophys. Res.*, **114**, C02005, doi:10.1029/2008JC005055.
- Tziperman, E., L. Zanna, and C. Penland, 2008: Nonnormal thermohaline circulation dynamics in a coupled ocean–atmosphere GCM. *J. Phys. Oceanogr.*, **38**, 588–604.
- Walker, A., and J. Pedlosky, 2002: Instability of meridional baroclinic currents. *J. Phys. Oceanogr.*, **32**, 1075–1093.
- Wang, J., 2011: Instabilities of an eastern boundary current with and without large-scale flow influence. Ph.D. thesis, Massachusetts Institute of Technology, 227 pp.
- White, W., 1977: Annual forcing of baroclinic long waves in the tropical North Pacific Ocean. *J. Phys. Oceanogr.*, **7**, 50–61.
- Winton, M., 1997: The damping effect of bottom topography on internal decadal-scale oscillations of the thermohaline circulation. *J. Phys. Oceanogr.*, **27**, 203–208.
- Wunsch, C., 1997: The vertical partition of oceanic horizontal kinetic energy. *J. Phys. Oceanogr.*, **27**, 1770–1794.
- Zanna, L., P. Heimbach, A. Moore, and E. Tziperman, 2011a: Upper ocean singular vectors of the North Atlantic climate with implications for linear predictability and variability. *Quart. J. Roy. Meteor. Soc.*, **138**, 500–513, doi:10.1002/qj.937.
- , —, —, and —, 2011b: Optimal excitation of interannual atlantic meridional overturning circulation variability. *J. Climate*, **24**, 413–427.
- Zhang, R., 2008: Coherent surface-subsurface fingerprint of the Atlantic meridional overturning circulation. *Geophys. Res. Lett.*, **35**, L20705, doi:10.1029/2008GL035463.
- , 2010: Latitudinal dependence of Atlantic Meridional overturning circulation (AMOC) variations. *Geophys. Res. Lett.*, **37**, L16703, doi:10.1029/2010GL044474.
- , T. Delworth, and I. Held, 2007: Can the Atlantic Ocean drive the observed multidecadal variability in the Northern Hemisphere mean temperature? *Geophys. Res. Lett.*, **34**, L02709, doi:10.1029/2006GL028683.